

The Boundary Element Method for Acoustic Transmission with Nonconforming Grids*

Elwin van 't Wout[†]

February 20, 2024

Abstract

Acoustic wave propagation through a homogeneous material embedded in an unbounded medium can be formulated as a boundary integral equation and accurately solved with the boundary element method. The computational efficiency deteriorates at high frequencies due to the increase in mesh size with a fixed number of elements per wavelength and also at high material contrasts due to the ill-conditioning of the linear system. This study presents the design of boundary element methods feasible for nonconforming surface meshes at the material interface. The nonconforming algorithm allows for independent grid generation, improves flexibility, and reduces the degrees of freedom. It works for different boundary integral formulations for Helmholtz transmission problems, operator preconditioning, and coupling with finite element solvers. The extensive numerical benchmarks at canonical configurations and an acoustic foam model confirm the significant improvements in computational efficiency when employing the nonconforming grid coupling in the boundary element method.

Keywords: computational acoustics, nonconforming grids, boundary element method, finite element method

1 Introduction

The boundary element method (BEM) is an efficient algorithm to numerically solve harmonic wave propagation in piecewise homogeneous materials. The algorithm allows for large-scale simulations in acoustics, electromagnetics, and elastodynamics, among other disciplines [1, 2]. A rich literature on fractional

*© 2024. This manuscript version is made available under the CC-BY-NC-ND 4.0 license. This manuscript is published in the Journal of Computational and Applied Mathematics in final form at <https://doi.org/10.1016/j.cam.2024.115838>.

[†]Institute for Mathematical and Computational Engineering, School of Engineering and Faculty of Mathematics, Pontificia Universidad Católica de Chile, Santiago, Chile. Contact: e.wout@uc.cl

Sobolev spaces supports its accuracy [3, 4, 5, 6]. The key distinction between the BEM and numerical methods such as finite differences and the finite element method (FEM) is the reformulation of the volumetric differential equation into boundary integral equations at the material interfaces. Green’s functions in the BEM guarantee accurate simulation of exterior scattering and wave transmission. Furthermore, accelerators such as the fast multipole method and hierarchical matrix compression efficiently compute large-scale problems on modern computer architectures. However, the BEM is limited to models that possess Green’s functions, thus restricting the applicability primarily to piecewise homogeneous materials with a linear response to the wave field.

This study considers acoustic wave transmission through a homogeneous material embedded in free space. Such configurations can be modelled by boundary integral formulations of the Helmholtz equation for the exterior and interior regions. The transmission conditions at the material interface couple the field representations into a surface potential problem. The different choices of representation formulas and surface potentials lead to a wealth of boundary integral formulations with specific computational characteristics [7]. The boundary integral equations are then numerically solved with Galerkin or collocation methods. The Galerkin discretisation requires a surface mesh, typically made of triangular elements [8]. Differently, collocation-based schemes such as Nyström discretisation [9, 10], isogeometric analysis [11, 12], and neural networks [13] do not require a triangularisation of the surface. This study considers Galerkin discretisation on triangular surface grids because of its meshing flexibility and mathematical solid foundation.

All boundary integral formulations for transmission problems involve a set of boundary integral operators based on the interior Green’s function and others based on the exterior wavenumber. The interior and exterior boundary integral representations must be coupled by enforcing some form of field continuity across the discrete representation of the material interface. This condition is relatively straightforward for conforming meshes, that is, a unique grid at each surface where the nodes, edges, and faces are consistent with the structure of neighbouring elements. However, this also means that the grid resolution has to be sufficiently fine to represent the smallest wavelength between the exterior and interior sides of each material interface. The novelty of this manuscript is the Galerkin discretisation of the exterior and interior operators on independent triangular surface meshes, which are then coupled by nonconforming grid projections. The added flexibility to the BEM’s design alleviates the mesh restrictions at the interface’s side with longer wavelength and improves the overall computational efficiency for transmission problems.

Nonconforming grids are widely used in numerical methods for partial differential equations such as the FEM. In those cases, two volumetric meshes for different subdomains are independently created so that the boundaries of these grids might not match at the common interface [14]. There are many stable and efficient algorithms to perform the data transfer between nonconforming meshes (cf. [15, 16]). Examples include interpolation [17], projection on Lagrange multipliers [18], and mortar techniques [19]. Allowing for nonconforming grids is

particularly beneficial to scenarios such as multiphysics models [20], contact problems [21], domain decomposition [22], and modular software design [23]. The nonconforming FEM also extends the feasible frequency range for acoustic transmission, compared to standard techniques with the same number of degrees of freedom [24].

There is a sharp contrast between the extensive literature and the impressive developments of nonconforming domain decomposition methods for differential equations compared to boundary integral equations. Furthermore, the techniques developed for the FEM cannot be applied directly to the BEM due to the reduction of the volumetric wave field to a surface potential. First, most nonconforming BEM techniques in the literature consider a different approach than those adopted in this manuscript. In those studies, the surface mesh is partitioned into separate surface patches that may not match at one-dimensional contours. Such surface-based domain decomposition approaches include mortar boundary elements [25, 26, 27], discontinuous Galerkin discretisation [28, 29, 30, 31, 32, 33, 34], Nitsche methods [35, 36, 37, 38], overlapping partitions [39], and multi-branch basis functions [40]. Second, this study neither follows the multi-domain approach of partitioning volumetric subdomains [41], leading to additional transmission interfaces. In contrast, the proposed algorithm does not decompose any geometric structure at all but instead uses two different meshes at the same physical surface. The reason for creating two meshes at each surface is that different boundary integral operators at the same interface can be assembled on another mesh, depending on the wavenumber of the Green's function involved. They are then coupled together with nonconforming grid projections. Techniques for such nonconforming BEM implementations have only recently been reported. A nonoverlapping domain decomposition method was designed for nonpenetrable objects [42] and extended to coatings [43], transmission problems [44, 45, 46], mixed basis functions [47], multiple traces formulations [48, 49], and numerical accelerators [50, 51]. The coupling matrices at the nonconforming interfaces are calculated with numerical quadrature on a union mesh or Lagrange multipliers [52]. Notice that all these references to literature concern Maxwell's equations for electromagnetics, not the Helmholtz equation. For acoustics, tearing and interconnecting techniques [53] perform volumetric domain decomposition but were applied to conforming meshes only.

This study presents the novel application of nonconforming BEM to the Helmholtz model for acoustic wave propagation. The proposed methodology in this study is distinctive from its electromagnetic counterparts. For instance, different basis functions, different boundary integral formulations, and a different mortar technique at nonconforming meshes will be presented, along with extensive computational benchmarks. Furthermore, the nonconforming BEM for acoustic transmission will be extended to operator preconditioning for screen problems and FEM-BEM coupling for heterogeneous materials. In the latter case, nonconforming techniques exist for FEM-BEM algorithms [54, 55, 56, 57, 58, 59, 60, 61] and the volume-surface integral equations [62, 63, 64], but all references use different algorithms than those presented in this manuscript. The

manuscript's scope is the algorithmic development of acoustic BEM on non-conforming grids, excluding the numerical analysis of the boundary integral formulations.

This study designs a BEM for acoustic transmission at piecewise homogeneous regions with nonconforming meshes at material interfaces. The boundary integral formulations will be presented in Section 2 and the nonconforming coupling algorithm in Section 3. Section 4 explains the extension to operator preconditioning and FEM-BEM coupling. Finally, the numerical benchmarks in Section 5 showcase the computational benefits of the nonconforming BEM.

2 Formulation

This study considers the propagation of harmonic acoustic waves in media with a linear response. A bounded domain $\Omega_{\text{int}} \subset \mathbb{R}^3$ with surface Γ is embedded in an unbounded exterior domain $\Omega_{\text{ext}} \subset \mathbb{R}^3$. The boundary is Lipschitz continuous with outward pointing unit normal $\hat{\mathbf{n}}$. The time dependency of wave propagation is extracted by assumming an $e^{-i\omega t}$ waveform, where ω denotes the angular frequency and i the imaginary unit. The known incident wave field p_{inc} has a frequency f . Let us denote the unknown acoustic field by p_{tot} and define the scattered field as $p_{\text{sca}} = p_{\text{tot}} - p_{\text{inc}}$. The mass density is denoted by ρ_{ext} and ρ_{int} , and the speed of sound by c_{ext} and c_{int} in the exterior and interior domains, respectively. They are all assumed to be constant. The exterior and interior wavenumbers are given by $k_{\text{ext}} = 2\pi f/c_{\text{ext}}$ and $k_{\text{int}} = 2\pi f/c_{\text{int}}$, respectively. The acoustic pressure field in such a configuration can accurately be described by the Helmholtz system

$$\begin{cases} \Delta p_{\text{tot}} + k_{\text{ext}}^2 p_{\text{tot}} = 0, & \text{in } \Omega_{\text{ext}}; \\ \Delta p_{\text{tot}} + k_{\text{int}}^2 p_{\text{tot}} = 0, & \text{in } \Omega_{\text{int}}; \\ \gamma_D^+ p_{\text{tot}} = \gamma_D^- p_{\text{tot}}, & \text{at } \Gamma; \\ \frac{1}{\rho_{\text{ext}}} \gamma_N^+ p_{\text{tot}} = \frac{1}{\rho_{\text{int}}} \gamma_N^- p_{\text{tot}}, & \text{at } \Gamma; \\ \lim_{\mathbf{r} \rightarrow \infty} |\mathbf{r}|(\partial_{|\mathbf{r}|} p_{\text{sca}} - i k_{\text{ext}} p_{\text{sca}}) = 0 \end{cases} \quad (1)$$

where Δ denotes the Laplace operator and

$$\gamma_D^+ p_{\text{tot}}(\mathbf{x}) = \lim_{\mathbf{y} \rightarrow \mathbf{x}} p_{\text{tot}}(\mathbf{y}), \quad \mathbf{x} \in \Gamma, \quad \mathbf{y} \in \Omega_{\text{ext}}, \quad (2a)$$

$$\gamma_D^- p_{\text{tot}}(\mathbf{x}) = \lim_{\mathbf{y} \rightarrow \mathbf{x}} p_{\text{tot}}(\mathbf{y}), \quad \mathbf{x} \in \Gamma, \quad \mathbf{y} \in \Omega_{\text{int}}, \quad (2b)$$

$$\gamma_N^+ p_{\text{tot}}(\mathbf{x}) = \lim_{\mathbf{y} \rightarrow \mathbf{x}} \nabla p_{\text{tot}}(\mathbf{y}) \cdot \hat{\mathbf{n}}(\mathbf{x}), \quad \mathbf{x} \in \Gamma, \quad \mathbf{y} \in \Omega_{\text{ext}}, \quad (2c)$$

$$\gamma_N^- p_{\text{tot}}(\mathbf{x}) = \lim_{\mathbf{y} \rightarrow \mathbf{x}} \nabla p_{\text{tot}}(\mathbf{y}) \cdot \hat{\mathbf{n}}(\mathbf{x}), \quad \mathbf{x} \in \Gamma, \quad \mathbf{y} \in \Omega_{\text{int}}, \quad (2d)$$

the Dirichlet and Neumann traces, respectively.

2.1 Boundary integral operators

Since the model considers a piecewise homogeneous material, the volumetric Helmholtz equation (1) can be rewritten into boundary integral equations on the material interface. More information on the design process of boundary integral formulations can be found in [7], where the same notation is used. Details on the functional analysis can be found in textbooks such as [3, 4, 5, 6].

Since this study introduces nonconforming meshes at material interfaces, the interior and exterior sides of the object's surface need to be distinguished. For this purpose, let us define Γ_{int} and Γ_{ext} the triangular surface meshes at Γ that will be used for the interior and exterior boundary integral operators, respectively. Here, only polyhedral surfaces will be considered so that the physical surfaces spanned by the meshes coincide with the material interfaces.

The operators mapping from the surface to volume are given by

$$[\mathcal{V}_{\text{int}}\psi](\mathbf{x}) = \iint_{\Gamma_{\text{int}}} G_{\text{int}}(\mathbf{x}, \mathbf{y})\psi(\mathbf{y}) \, d\mathbf{y} \quad \text{for } \mathbf{x} \in \Omega_{\text{int}}; \quad (3a)$$

$$[\mathcal{V}_{\text{ext}}\psi](\mathbf{x}) = \iint_{\Gamma_{\text{ext}}} G_{\text{ext}}(\mathbf{x}, \mathbf{y})\psi(\mathbf{y}) \, d\mathbf{y} \quad \text{for } \mathbf{x} \in \Omega_{\text{ext}}; \quad (3b)$$

$$[\mathcal{K}_{\text{int}}\phi](\mathbf{x}) = \iint_{\Gamma_{\text{int}}} \frac{\partial G_{\text{int}}(\mathbf{x}, \mathbf{y})}{\partial \hat{\mathbf{n}}(\mathbf{y})} \phi(\mathbf{y}) \, d\mathbf{y} \quad \text{for } \mathbf{x} \in \Omega_{\text{int}}; \quad (3c)$$

$$[\mathcal{K}_{\text{ext}}\phi](\mathbf{x}) = \iint_{\Gamma_{\text{ext}}} \frac{\partial G_{\text{ext}}(\mathbf{x}, \mathbf{y})}{\partial \hat{\mathbf{n}}(\mathbf{y})} \phi(\mathbf{y}) \, d\mathbf{y} \quad \text{for } \mathbf{x} \in \Omega_{\text{ext}}; \quad (3d)$$

the single-layer and double-layer potential integral operators, respectively. Here,

$$G_{\text{int}}(\mathbf{x}, \mathbf{y}) = \frac{e^{ik_{\text{int}}|\mathbf{x}-\mathbf{y}|}}{4\pi|\mathbf{x}-\mathbf{y}|}, \quad \mathbf{x}, \mathbf{y} \in \Omega_{\text{int}}, \, \mathbf{x} \neq \mathbf{y}; \quad (4a)$$

$$G_{\text{ext}}(\mathbf{x}, \mathbf{y}) = \frac{e^{ik_{\text{ext}}|\mathbf{x}-\mathbf{y}|}}{4\pi|\mathbf{x}-\mathbf{y}|}, \quad \mathbf{x}, \mathbf{y} \in \Omega_{\text{ext}}, \, \mathbf{x} \neq \mathbf{y} \quad (4b)$$

denote the Green's functions with the wavenumber of the interior and exterior region, respectively. Furthermore,

$$[\mathcal{V}_{\text{ext}}\psi](\mathbf{x}) = \iint_{\Gamma_{\text{ext}}} G_{\text{ext}}(\mathbf{x}, \mathbf{y})\psi(\mathbf{y}) \, d\mathbf{y} \quad \text{for } \mathbf{x} \in \Gamma_{\text{ext}}; \quad (5a)$$

$$[\mathcal{K}_{\text{ext}}\phi](\mathbf{x}) = \iint_{\Gamma_{\text{ext}}} \frac{\partial}{\partial \hat{\mathbf{n}}(\mathbf{y})} G_{\text{ext}}(\mathbf{x}, \mathbf{y})\phi(\mathbf{y}) \, d\mathbf{y} \quad \text{for } \mathbf{x} \in \Gamma_{\text{ext}}; \quad (5b)$$

$$[\mathcal{T}_{\text{ext}}\psi](\mathbf{x}) = \frac{\partial}{\partial \hat{\mathbf{n}}(\mathbf{x})} \iint_{\Gamma_{\text{ext}}} G_{\text{ext}}(\mathbf{x}, \mathbf{y})\psi(\mathbf{y}) \, d\mathbf{y} \quad \text{for } \mathbf{x} \in \Gamma_{\text{ext}}; \quad (5c)$$

$$[\mathcal{D}_{\text{ext}}\phi](\mathbf{x}) = -\frac{\partial}{\partial \hat{\mathbf{n}}(\mathbf{x})} \iint_{\Gamma_{\text{ext}}} \frac{\partial}{\partial \hat{\mathbf{n}}(\mathbf{y})} G_{\text{ext}}(\mathbf{x}, \mathbf{y})\phi(\mathbf{y}) \, d\mathbf{y} \quad \text{for } \mathbf{x} \in \Gamma_{\text{ext}}; \quad (5d)$$

which are called the exterior single-layer, double-layer, adjoint double-layer and hypersingular boundary integral operators, respectively. The interior boundary

integral operators are defined equivalently but with the interior Green's function and the interior surface mesh. Remember that the normal is always pointing outwards, regardless of the operator.

With the distinction between interior and exterior meshes, the following identity mappings need to be introduced:

$$\begin{aligned} I_{\text{ext}} : \Gamma_{\text{ext}} &\rightarrow \Gamma_{\text{ext}}, \\ \varphi_{\text{ext}} &\mapsto \varphi_{\text{ext}}; \end{aligned} \tag{6a}$$

$$\begin{aligned} I_{\text{int}} : \Gamma_{\text{int}} &\rightarrow \Gamma_{\text{int}}, \\ \varphi_{\text{int}} &\mapsto \varphi_{\text{int}}; \end{aligned} \tag{6b}$$

$$\begin{aligned} Z_{\text{ext}} : \Gamma_{\text{ext}} &\rightarrow \Gamma, \\ \varphi_{\text{ext}} &\mapsto \varphi_{\text{ext}}; \end{aligned} \tag{6c}$$

$$\begin{aligned} Z_{\text{int}} : \Gamma_{\text{int}} &\rightarrow \Gamma, \\ \varphi_{\text{int}} &\mapsto \varphi_{\text{int}}. \end{aligned} \tag{6d}$$

The first two operators are standard identity operators acting on the exterior or interior surface mesh, respectively. The last two operators are transmission operators that formally represent an identity mapping from the exterior or interior surface mesh towards the physical surface. Hence, the operator $Z_{\text{int}}^{-1} Z_{\text{ext}}$ maps a function on the exterior mesh towards itself on the interior mesh.

2.2 Direct boundary integral formulations

Let us consider the following definitions of the unknown interior and exterior fields:

$$u_{\text{int}} = \begin{cases} 0 & \text{in } \Omega_{\text{ext}}, \\ p_{\text{tot}} & \text{in } \Omega_{\text{int}}; \end{cases} \tag{7a}$$

$$u_{\text{ext}} = \begin{cases} p_{\text{tot}} - p_{\text{inc}} & \text{in } \Omega_{\text{ext}}, \\ -p_{\text{inc}} & \text{in } \Omega_{\text{int}}; \end{cases} \tag{7b}$$

which are the interior field and the scattered field, respectively. These fields can be represented as

$$u_{\text{int}} = \mathcal{V}_{\text{int}} \psi_{\text{int}} - \mathcal{K}_{\text{int}} \phi_{\text{int}} \quad \text{in } \mathbb{R}^3 \setminus \Gamma, \tag{8a}$$

$$u_{\text{ext}} = \mathcal{V}_{\text{ext}} \psi_{\text{ext}} - \mathcal{K}_{\text{ext}} \phi_{\text{ext}} \quad \text{in } \mathbb{R}^3 \setminus \Gamma, \tag{8b}$$

in terms of the unknown surface potentials

$$\phi_{\text{int}} = \gamma_D^- p_{\text{tot}} \quad \text{on } \Gamma_{\text{int}}, \tag{9a}$$

$$\psi_{\text{int}} = \gamma_N^- p_{\text{tot}} \quad \text{on } \Gamma_{\text{int}}, \tag{9b}$$

$$\phi_{\text{ext}} = -\gamma_D^+ p_{\text{tot}} \quad \text{on } \Gamma_{\text{ext}}, \tag{9c}$$

$$\psi_{\text{ext}} = -\gamma_N^+ p_{\text{tot}} \quad \text{on } \Gamma_{\text{ext}}. \tag{9d}$$

Hence, the transmission conditions read

$$-Z_{\text{ext}}\phi_{\text{ext}} = Z_{\text{int}}\phi_{\text{int}} \quad \text{on } \Gamma; \quad (10a)$$

$$-\frac{1}{\rho_{\text{ext}}}Z_{\text{ext}}\psi_{\text{ext}} = \frac{1}{\rho_{\text{int}}}Z_{\text{int}}\psi_{\text{int}} \quad \text{on } \Gamma. \quad (10b)$$

The traces of the representation formulas read

$$\left(\frac{1}{2}I_{\text{int}} - A_{\text{int}}\right) \begin{bmatrix} \phi_{\text{int}} \\ \psi_{\text{int}} \end{bmatrix} = \begin{bmatrix} 0 \\ 0 \end{bmatrix} \quad \text{on } \Gamma_{\text{int}}, \quad (11a)$$

$$\left(-\frac{1}{2}I_{\text{ext}} - A_{\text{ext}}\right) \begin{bmatrix} \phi_{\text{ext}} \\ \psi_{\text{ext}} \end{bmatrix} = \begin{bmatrix} \gamma_D^+ u_{\text{inc}} \\ \gamma_N^+ u_{\text{inc}} \end{bmatrix} \quad \text{on } \Gamma_{\text{ext}}, \quad (11b)$$

for the Calderón systems

$$A_{\text{int}} = \begin{bmatrix} -K_{\text{int}} & V_{\text{int}} \\ D_{\text{int}} & T_{\text{int}} \end{bmatrix}, \quad (12a)$$

$$A_{\text{ext}} = \begin{bmatrix} -K_{\text{ext}} & V_{\text{ext}} \\ D_{\text{ext}} & T_{\text{ext}} \end{bmatrix}. \quad (12b)$$

Notice that the transmission conditions (10) yield two linear equations and the Calderón systems (11) another four linear equations, all with respect to four unknown potentials (9). The design of consistent boundary integral formulations follows different combinations of these model equations, as will be presented below.

2.2.1 Multiple-traces formulation

Substituting the identity operators in the Calderón systems (11) by the interface conditions (10) gives the system

$$\begin{bmatrix} -K_{\text{ext}} & V_{\text{ext}} & \frac{1}{2}Z_{\text{ext}}^{-1}Z_{\text{int}} & 0 \\ D_{\text{ext}} & T_{\text{ext}} & 0 & \frac{1}{2}\frac{\rho_{\text{ext}}}{\rho_{\text{int}}}Z_{\text{ext}}^{-1}Z_{\text{int}} \\ -\frac{1}{2}Z_{\text{int}}^{-1}Z_{\text{ext}} & 0 & -K_{\text{int}} & V_{\text{int}} \\ 0 & -\frac{1}{2}\frac{\rho_{\text{int}}}{\rho_{\text{ext}}}Z_{\text{int}}^{-1}Z_{\text{ext}} & D_{\text{int}} & T_{\text{int}} \end{bmatrix} \begin{bmatrix} \phi_{\text{ext}} \\ \psi_{\text{ext}} \\ \phi_{\text{int}} \\ \psi_{\text{int}} \end{bmatrix} = \begin{bmatrix} -\gamma_D^+ u_{\text{inc}} \\ -\gamma_N^+ u_{\text{inc}} \\ 0 \\ 0 \end{bmatrix} \quad (13)$$

which is called the multiple-traces formulation (MTF) [65].

2.2.2 Single-trace formulations

The single-trace formulations use a single set of Dirichlet and Neumann traces at the boundary. Specifically,

$$\phi = -\phi_{\text{ext}} = Z_{\text{ext}}^{-1}Z_{\text{int}}\phi_{\text{int}}, \quad \text{on } \Gamma_{\text{ext}}; \quad (14a)$$

$$\psi = -\psi_{\text{ext}} = \frac{\rho_{\text{ext}}}{\rho_{\text{int}}}Z_{\text{ext}}^{-1}Z_{\text{int}}\psi_{\text{int}}, \quad \text{on } \Gamma_{\text{ext}}, \quad (14b)$$

where the equalities follow from the transmission conditions. Substituting these traces in the interior Calderón system (11a) yields

$$\left(\frac{1}{2}I_{\text{int}} - \hat{A}_{\text{int}}\right) \begin{bmatrix} Z_{\text{int}}^{-1}Z_{\text{ext}}\phi \\ Z_{\text{int}}^{-1}Z_{\text{ext}}\psi \end{bmatrix} = \begin{bmatrix} 0 \\ 0 \end{bmatrix} \quad (15)$$

where

$$\hat{A}_{\text{int}} = \begin{bmatrix} -K_{\text{int}} & \frac{\rho_{\text{int}}}{\rho_{\text{ext}}}V_{\text{int}} \\ \frac{\rho_{\text{ext}}}{\rho_{\text{int}}}D_{\text{int}} & T_{\text{int}} \end{bmatrix} \quad (16)$$

a scaled Calderón operator. Notice that the interior equation (15) maps potentials on the exterior mesh to the interior mesh. For consistency, and to accomodate combined field equations, let us consider

$$Z_{\text{ext}}^{-1}Z_{\text{int}} \left(\frac{1}{2}I_{\text{int}} - \hat{A}_{\text{int}}\right) Z_{\text{int}}^{-1}Z_{\text{ext}} \begin{bmatrix} \phi \\ \psi \end{bmatrix} = \begin{bmatrix} 0 \\ 0 \end{bmatrix} \quad \text{on } \Gamma_{\text{ext}}, \quad (17a)$$

$$\left(\frac{1}{2}I_{\text{ext}} + A_{\text{ext}}\right) \begin{bmatrix} \phi \\ \psi \end{bmatrix} = \begin{bmatrix} \gamma_D^+ u_{\text{inc}} \\ \gamma_N^+ u_{\text{inc}} \end{bmatrix} \quad \text{on } \Gamma_{\text{ext}}, \quad (17b)$$

which are called the interior and exterior single-trace Calderón systems, respectively. They consist of four linear equations for two unknown potentials. Hence, linear combinations yield different boundary integral equations. Taking the difference of the exterior and interior Calderón systems yields

$$\frac{1}{2} (I_{\text{ext}} - Z_{\text{ext}}^{-1}Z_{\text{int}}I_{\text{int}}Z_{\text{int}}^{-1}Z_{\text{ext}}) \begin{bmatrix} \phi \\ \psi \end{bmatrix} + (A_{\text{ext}} + Z_{\text{ext}}^{-1}Z_{\text{int}}\hat{A}_{\text{int}}Z_{\text{int}}^{-1}Z_{\text{ext}}) \begin{bmatrix} \phi \\ \psi \end{bmatrix} = \begin{bmatrix} \gamma_D^+ u_{\text{inc}} \\ \gamma_N^+ u_{\text{inc}} \end{bmatrix}.$$

The first term is zero (except for numerical errors) so that

$$(A_{\text{ext}} + Z_{\text{ext}}^{-1}Z_{\text{int}}\hat{A}_{\text{int}}Z_{\text{int}}^{-1}Z_{\text{ext}}) \begin{bmatrix} \phi \\ \psi \end{bmatrix} = \begin{bmatrix} \gamma_D^+ u_{\text{inc}} \\ \gamma_N^+ u_{\text{inc}} \end{bmatrix} \quad \text{on } \Gamma_{\text{ext}}, \quad (18)$$

which is called the exterior PMCHWT formulation after the inventors of its electromagnetic variant: Poggio-Miller-Chang-Harrington-Wu-Tsai [66, 67, 68], and also known as the Costabel-Stephan formulation [69]. Alternatively, taking the sum of the exterior and interior Calderón systems yields

$$\frac{1}{2} (I_{\text{ext}} + Z_{\text{ext}}^{-1}Z_{\text{int}}I_{\text{int}}Z_{\text{int}}^{-1}Z_{\text{ext}}) \begin{bmatrix} \phi \\ \psi \end{bmatrix} + (A_{\text{ext}} - Z_{\text{ext}}^{-1}Z_{\text{int}}\hat{A}_{\text{int}}Z_{\text{int}}^{-1}Z_{\text{ext}}) \begin{bmatrix} \phi \\ \psi \end{bmatrix} = \begin{bmatrix} \gamma_D^+ u_{\text{inc}} \\ \gamma_N^+ u_{\text{inc}} \end{bmatrix}.$$

Assuming exact projection of the identity operator,

$$I_{\text{ext}} + (A_{\text{ext}} - Z_{\text{ext}}^{-1}Z_{\text{int}}\hat{A}_{\text{int}}Z_{\text{int}}^{-1}Z_{\text{ext}}) \begin{bmatrix} \phi \\ \psi \end{bmatrix} = \begin{bmatrix} \gamma_D^+ u_{\text{inc}} \\ \gamma_N^+ u_{\text{inc}} \end{bmatrix} \quad \text{on } \Gamma_{\text{ext}}, \quad (19)$$

which is called the exterior Müller formulation [70], and also known as the Kress-Roach formulation [71].

Interior variant Other variants of single-trace formulations use the interior potentials

$$\phi = \phi_{\text{int}} = -Z_{\text{int}}^{-1} Z_{\text{ext}} \phi_{\text{ext}}, \quad \text{on } \Gamma_{\text{int}}; \quad (20a)$$

$$\psi = \psi_{\text{int}} = -\frac{\rho_{\text{int}}}{\rho_{\text{ext}}} Z_{\text{int}}^{-1} Z_{\text{ext}} \psi_{\text{ext}}, \quad \text{on } \Gamma_{\text{int}}. \quad (20b)$$

Then, the interior PMCHWT formulation reads

$$\left(Z_{\text{int}}^{-1} Z_{\text{ext}} \hat{A}_{\text{ext}} Z_{\text{ext}}^{-1} Z_{\text{int}} + A_{\text{int}} \right) \begin{bmatrix} \phi \\ \psi \end{bmatrix} = Z_{\text{int}}^{-1} Z_{\text{ext}} \begin{bmatrix} \gamma_D^+ u_{\text{inc}} \\ \frac{\rho_{\text{int}}}{\rho_{\text{ext}}} \gamma_N^+ u_{\text{inc}} \end{bmatrix} \quad \text{on } \Gamma_{\text{int}}, \quad (21)$$

and

$$I_{\text{int}} + \left(Z_{\text{int}}^{-1} Z_{\text{ext}} \hat{A}_{\text{ext}} Z_{\text{ext}}^{-1} Z_{\text{int}} - A_{\text{int}} \right) \begin{bmatrix} \phi \\ \psi \end{bmatrix} = Z_{\text{int}}^{-1} Z_{\text{ext}} \begin{bmatrix} \gamma_D^+ u_{\text{inc}} \\ \frac{\rho_{\text{int}}}{\rho_{\text{ext}}} \gamma_N^+ u_{\text{inc}} \end{bmatrix} \quad \text{on } \Gamma_{\text{int}}, \quad (22)$$

is the interior Müller formulation, where

$$\hat{A}_{\text{ext}} = \begin{bmatrix} -K_{\text{ext}} & \frac{\rho_{\text{ext}}}{\rho_{\text{int}}} V_{\text{ext}} \\ \frac{\rho_{\text{int}}}{\rho_{\text{ext}}} D_{\text{ext}} & T_{\text{ext}} \end{bmatrix}$$

a scaled Calderón operator.

2.3 Indirect boundary integral formulations

The representation formulas (8) directly give boundary integral formulations in terms of unknown surface potentials that represent acoustic field traces. Indirect representation formulas follow a different approach and define surface potentials that do not necessarily have a direct physical interpretation, here denoted by μ and ν . Among the many options (cf. [7]), let us consider the high-contrast formulations [72]. In the following, superscript circles denote passage through the opposite mesh as

$$\overset{\circ}{X}_{\text{ext}} = Z_{\text{int}}^{-1} Z_{\text{ext}} X_{\text{ext}} Z_{\text{ext}}^{-1} Z_{\text{int}}, \quad (23a)$$

$$\overset{\circ}{X}_{\text{int}} = Z_{\text{ext}}^{-1} Z_{\text{int}} X_{\text{int}} Z_{\text{int}}^{-1} Z_{\text{ext}} \quad (23b)$$

for X any of the boundary integral operators. Now, the representation formulas

$$u_{\text{int}} = \mathcal{V}_{\text{int}} \psi_{\text{int}} - \mathcal{K}_{\text{int}} \phi_{\text{int}}, \quad (24a)$$

$$u_{\text{ext}} = \mathcal{V}_{\text{ext}} \mu_{\text{ext}}, \quad (24b)$$

yield the system

$$\begin{bmatrix} \frac{1}{2} I_{\text{ext}} - \overset{\circ}{T}_{\text{int}} & -\frac{\rho_{\text{ext}}}{\rho_{\text{int}}} \overset{\circ}{D}_{\text{int}} V_{\text{ext}} \\ I_{\text{ext}} & \frac{1}{2} I_{\text{ext}} - T_{\text{ext}} \end{bmatrix} \begin{bmatrix} \gamma_N^+ p_{\text{tot}} \\ \mu_{\text{ext}} \end{bmatrix} = \begin{bmatrix} \frac{\rho_{\text{ext}}}{\rho_{\text{int}}} \overset{\circ}{D}_{\text{int}} \gamma_D^+ u_{\text{inc}} \\ \gamma_N^+ u_{\text{inc}} \end{bmatrix} \quad \text{on } \Gamma_{\text{ext}}, \quad (25)$$

called the exterior high-contrast Neumann formulation. The representation formulas

$$u_{\text{int}} = \mathcal{V}_{\text{int}} \psi_{\text{int}} - \mathcal{K}_{\text{int}} \phi_{\text{int}}, \quad (26a)$$

$$u_{\text{ext}} = -\mathcal{K}_{\text{ext}} \nu_{\text{ext}} \quad (26b)$$

yield the system

$$\begin{bmatrix} \frac{1}{2}I_{\text{ext}} + K_{\text{ext}} & I_{\text{ext}} \\ -\frac{\rho_{\text{int}}}{\rho_{\text{ext}}} \mathring{V}_{\text{int}} D_{\text{ext}} & \frac{1}{2}I_{\text{ext}} + \mathring{K}_{\text{int}} \end{bmatrix} \begin{bmatrix} \nu_{\text{ext}} \\ \gamma_D^+ u_{\text{tot}} \end{bmatrix} = \begin{bmatrix} \gamma_D^+ u_{\text{inc}} \\ \frac{\rho_{\text{int}}}{\rho_{\text{ext}}} \mathring{V}_{\text{int}} \gamma_N^+ u_{\text{inc}} \end{bmatrix} \quad \text{on } \Gamma_{\text{ext}}, \quad (27)$$

called the exterior high-contrast Dirichlet formulation. The representation formulas

$$u_{\text{int}} = \mathcal{V}_{\text{int}} \mu_{\text{int}}, \quad (28a)$$

$$u_{\text{ext}} = \mathcal{V}_{\text{ext}} \psi_{\text{ext}} - \mathcal{K}_{\text{ext}} \phi_{\text{ext}} \quad (28b)$$

yield the system

$$\begin{bmatrix} \frac{1}{2}I_{\text{int}} + \mathring{T}_{\text{ext}} & \frac{\rho_{\text{int}}}{\rho_{\text{ext}}} \mathring{D}_{\text{ext}} V_{\text{int}} \\ -I_{\text{int}} & \frac{1}{2}I_{\text{int}} + T_{\text{int}} \end{bmatrix} \begin{bmatrix} \gamma_N^- u_{\text{tot}} \\ \mu_{\text{int}} \end{bmatrix} = \begin{bmatrix} \frac{\rho_{\text{int}}}{\rho_{\text{ext}}} Z_{\text{int}}^{-1} Z_{\text{ext}} (D_{\text{ext}} \gamma_D^+ u_{\text{inc}} + (\frac{1}{2}I_{\text{ext}} + T_{\text{ext}}) \gamma_N^+ u_{\text{inc}}) \\ 0 \end{bmatrix} \quad \text{on } \Gamma_{\text{int}}, \quad (29)$$

called the interior high-contrast Neumann formulation. Finally, the representation formulas

$$u_{\text{int}} = -\mathcal{K}_{\text{int}} \nu_{\text{int}}, \quad (30a)$$

$$u_{\text{ext}} = \mathcal{V}_{\text{ext}} \psi_{\text{ext}} - \mathcal{K}_{\text{ext}} \phi_{\text{ext}} \quad (30b)$$

yield the system

$$\begin{bmatrix} \frac{1}{2}I_{\text{int}} - K_{\text{int}} & -I_{\text{int}} \\ \frac{\rho_{\text{ext}}}{\rho_{\text{int}}} \mathring{V}_{\text{ext}} D_{\text{int}} & \frac{1}{2}I_{\text{int}} - \mathring{K}_{\text{ext}} \end{bmatrix} \begin{bmatrix} \nu_{\text{int}} \\ \gamma_D^- u_{\text{tot}} \end{bmatrix} = \begin{bmatrix} 0 \\ Z_{\text{int}}^{-1} Z_{\text{ext}} (V_{\text{ext}} \gamma_N^+ u_{\text{inc}} + (\frac{1}{2}I_{\text{ext}} - K_{\text{ext}}) \gamma_D^+ u_{\text{inc}}) \end{bmatrix} \quad \text{on } \Gamma_{\text{int}}, \quad (31)$$

called the interior high-contrast Dirichlet formulation.

2.4 Numerical discretisation

The discretisation of the boundary integral operators follows a standard Galerkin method [8]. All test and basis functions are continuous piecewise linear (P1) Lagrange polynomials, with value one in a specific grid node and zero in all other nodes of the triangular surface mesh.

3 Nonconforming grid projections

This study considers the acoustic transmission at a homogeneous domain with surface Γ , where two surface meshes Γ_{int} and Γ_{ext} are independently generated and the interior and exterior boundary integral operators are assembled on the respective triangulations. Each individual mesh is assumed to be conforming and to cover the physical surface Γ exactly. However, the grid Γ_{int} might not be conforming with Γ_{ext} , as depicted in Figure 1. Hence, let us denote the number of nodes in the interior and exterior mesh by N_{int} and N_{ext} , respectively. They are also the number of degrees of freedom in the discrete P1 spaces.

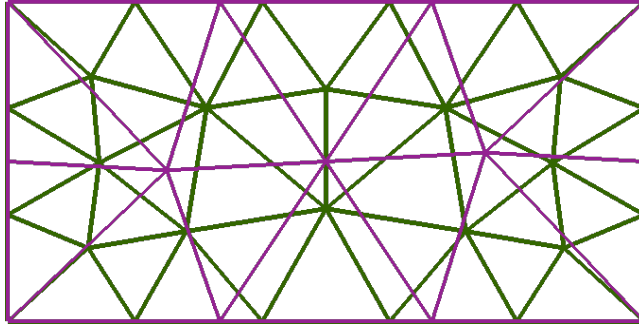


Figure 1: An example of two nonconforming triangular grids generated on the same rectangular domain.

3.1 Mortar matrices

Since all dense boundary integral operators in the models are defined with test and basis functions on the same mesh, these can be assembled with a standard weak formulation. Differently, the transmission operators (6c) and (6d) map between different meshes on the same surface. For example, one formally has

$$[Z_{\text{int}}\varphi_{\text{int}}](\mathbf{x}) = [Z_{\text{ext}}\varphi_{\text{ext}}](\mathbf{x}) \text{ for } \mathbf{x} \in \Gamma, \quad (32)$$

where φ_{int} and φ_{ext} are functions with the same values but defined on the meshes Γ_{int} and Γ_{ext} , respectively. Within the boundary integral formulations, these mortar operators are present in the form of $\varphi_{\text{int}} = Z_{\text{int}}^{-1}Z_{\text{ext}}\varphi_{\text{ext}}$, which represents an identity mapping from the exterior to the interior mesh. The weak formulation of this equation reads

$$\langle I_{\text{int}}\varphi_{\text{int}}, \theta_{\text{int}} \rangle_{\Gamma_{\text{int}}} = \langle Z_{\text{int}}^{-1}Z_{\text{ext}}\varphi_{\text{ext}}, \theta_{\text{int}} \rangle_{\Gamma_{\text{int}}} \quad (33)$$

with a standard L^2 inner product. The interior identity operator was included for clarity. The discrete version, i.e., substituting basis and test functions, of this weak formulation is a set of linear equations given by

$$\mathbf{M}_{\text{int}}\mathbf{v}_{\text{int}} = \mathbf{P}_{\text{int,ext}}\mathbf{v}_{\text{ext}} \quad (34)$$

where \mathbf{v}_{int} and \mathbf{v}_{ext} denote coefficient vectors on the interior and exterior mesh, respectively. The interior mass matrix \mathbf{M}_{int} has size $N_{\text{int}} \times N_{\text{int}}$ and element (i, j) corresponds to the inner product of test function i and basis function j on the interior mesh. Differently, the mortar matrix $\mathbf{P}_{\text{int,ext}}$ has size $N_{\text{int}} \times N_{\text{ext}}$ and element (i, j) corresponds to the inner product of test function i on the interior mesh and basis function j on the exterior mesh. These inner products are well defined since both meshes share the same physical surface. Finally, $\mathbf{P}_{\text{ext,int}}$ denotes the mortar matrix that maps from the interior to the exterior mesh and is the transpose of $\mathbf{P}_{\text{int,ext}}$.

3.2 Advancing front method

Volumetric domain decomposition techniques often require the computation of the same mortar matrix $\mathbf{P}_{\text{int,ext}}$. As mentioned in the introduction, many different algorithms exist to compute these matrices. Here, the *Projection Algorithm for Nonmatching Grids* (PANG) will be used [73]. This is an advancing front method that calculates the mortar matrix of P1 elements on nonconforming triangular surface meshes. This algorithm advances through the nonconforming grids by iteratively calculating triangle intersections, mortar contributions, and candidate neighbours. The reasons to use this specific algorithm are as follows. Firstly, open-source code of the algorithm is available [73]. Secondly, the algorithm has linear computational complexity [74]. Thirdly, it is robust in finite precision [75]. Fourthly, the necessary triangle connectivity tables are already available in the standard mesh formats used in the BEM. Here, no modifications to the PANG were made since it directly calculates the mortar matrices $\mathbf{P}_{\text{int,ext}}$ and $\mathbf{P}_{\text{ext,int}}$.

3.3 Discrete boundary integral formulations

With the mortar matrices available, the discretised boundary integral formulations can readily be obtained. The discrete MTF (13) reads

$$\begin{bmatrix} -\mathbf{K}_{\text{ext}} & \mathbf{V}_{\text{ext}} & \frac{1}{2}\mathbf{P}_{\text{ext,int}} & 0 \\ \mathbf{D}_{\text{ext}} & \mathbf{T}_{\text{ext}} & 0 & \frac{1}{2}\frac{\rho_{\text{ext}}}{\rho_{\text{int}}}\mathbf{P}_{\text{ext,int}} \\ -\frac{1}{2}\mathbf{P}_{\text{int,ext}} & 0 & -\mathbf{K}_{\text{int}} & \mathbf{V}_{\text{int}} \\ 0 & -\frac{1}{2}\frac{\rho_{\text{int}}}{\rho_{\text{ext}}}\mathbf{P}_{\text{int,ext}} & \mathbf{D}_{\text{int}} & \mathbf{T}_{\text{int}} \end{bmatrix} \begin{bmatrix} \mathbf{v}_{\text{ext}} \\ \mathbf{w}_{\text{ext}} \\ \mathbf{v}_{\text{int}} \\ \mathbf{w}_{\text{int}} \end{bmatrix} = \begin{bmatrix} -\mathbf{f} \\ -\mathbf{g} \\ \mathbf{0} \\ \mathbf{0} \end{bmatrix} \quad (35)$$

where the boldface operators denote the weak formulation of the corresponding boundary integral operators. The discrete PMCHWT formulation (18) reads

$$\begin{bmatrix} -\mathbf{K}_{\text{ext}} - \widehat{\mathbf{K}}_{\text{int}} & \mathbf{V}_{\text{ext}} + \widehat{\mathbf{V}}_{\text{int}} \\ \mathbf{D}_{\text{ext}} + \widehat{\mathbf{D}}_{\text{int}} & \mathbf{T}_{\text{ext}} + \widehat{\mathbf{T}}_{\text{int}} \end{bmatrix} \begin{bmatrix} \mathbf{v}_{\text{ext}} \\ \mathbf{w}_{\text{ext}} \end{bmatrix} = \begin{bmatrix} \mathbf{f} \\ \mathbf{g} \end{bmatrix} \quad (36)$$

where the superscript hat denotes the transformation

$$\widehat{\mathbf{V}}_{\text{int}} = \mathbf{P}_{\text{ext,int}} \mathbf{M}_{\text{int}}^{-1} \mathbf{V}_{\text{int}} \mathbf{M}_{\text{int}}^{-1} \mathbf{P}_{\text{int,ext}}. \quad (37)$$

Notice that the inverse mass matrices are necessary for coupling the discrete spaces of the operator products (cf. [76]). The discrete high-contrast formulation (25) reads

$$\begin{bmatrix} \frac{1}{2}\mathbf{M}_{\text{ext}} - \widehat{\mathbf{T}}_{\text{int}} & -\frac{\rho_{\text{ext}}}{\rho_{\text{int}}}\widehat{\mathbf{D}}_{\text{int}}\mathbf{M}_{\text{ext}}^{-1}\mathbf{V}_{\text{ext}} \\ \mathbf{M}_{\text{ext}} & \frac{1}{2}\mathbf{M}_{\text{ext}} - \mathbf{T}_{\text{ext}} \end{bmatrix} \begin{bmatrix} \gamma_N^+ p_{\text{tot}} \\ \psi_{\text{ext}} \end{bmatrix} = \begin{bmatrix} \frac{\rho_{\text{ext}}}{\rho_{\text{int}}}\widehat{\mathbf{D}}_{\text{int}}\mathbf{f} \\ \mathbf{g} \end{bmatrix}. \quad (38)$$

All other formulations can be discretised similarly.

The discrete formulations mentioned above are all weak forms. Mass-matrix preconditioning yields the strong form, i.e., multiplying the discrete equations from the left with the matrices

$$\begin{bmatrix} \mathbf{M}_{\text{ext}}^{-1} & 0 \\ 0 & \mathbf{M}_{\text{ext}}^{-1} \end{bmatrix}$$

for the single-trace and high-contrast formulations and

$$\begin{bmatrix} \mathbf{M}_{\text{ext}}^{-1} & 0 & 0 & 0 \\ 0 & \mathbf{M}_{\text{ext}}^{-1} & 0 & 0 \\ 0 & 0 & \mathbf{M}_{\text{int}}^{-1} & 0 \\ 0 & 0 & 0 & \mathbf{M}_{\text{int}}^{-1} \end{bmatrix}$$

for the MTF. Alternatively, more elaborate preconditioning strategies such as Calderón and OSRC preconditioning [7] can be applied as usual.

4 Extensions

Section 2 presented the nonconforming BEM for acoustic transmission at a single homogeneous material embedded in free space. The extension to multiple scattering at disjoint objects is straightforward. Another use case of nonconforming BEM is efficient parameter studies: when the wavespeed in one of the subdomains changes, one only needs to reassemble the operators in that domain while keeping all other boundary integral operators. This section explains other interesting applications: FEM-BEM coupling and operator preconditioning.

4.1 FEM-BEM coupling

Let us consider a heterogeneous material embedded in an unbounded homogeneous medium. The Helmholtz equation in the interior is given by

$$-\rho_{\text{int}} \nabla \cdot \left(\frac{1}{\rho_{\text{int}}} \nabla p_{\text{int}} \right) - k_{\text{int}}^2 p_{\text{int}} = 0 \quad (39)$$

where $\rho_{\text{int}}(\mathbf{x})$ and $k_{\text{int}}(\mathbf{x}) = 2\pi f / c_{\text{int}}(\mathbf{x})$ for $\mathbf{x} \in \Omega_{\text{int}}$ smooth functions. Its weak formulation (cf. [4]) reads

$$\begin{aligned} & \iiint_{\Omega_{\text{int}}} \frac{1}{\rho_{\text{int}}(\mathbf{x})} \nabla p_{\text{int}}(\mathbf{x}) \nabla (\rho_{\text{int}}(\mathbf{x}) q(\mathbf{x})) \, d\mathbf{x} - \iint_{\Gamma_{\text{int}}} \gamma_N^- p_{\text{int}}(\mathbf{x}) \gamma_D^- q(\mathbf{x}) \, d\mathbf{x} \\ & - \iiint_{\Omega_{\text{int}}} k_{\text{int}}^2(\mathbf{x}) p_{\text{int}}(\mathbf{x}) q(\mathbf{x}) \, d\mathbf{x} = 0, \end{aligned} \quad (40)$$

where q denotes the test function. The discretisation uses node-based continuous piecewise linear (P1) Lagrange basis and test functions on a tetrahedral grid. The exterior Calderón system (11b) yields

$$\left(\frac{1}{2}I_{\text{ext}} - K_{\text{ext}}\right) \gamma_D^+ p_{\text{tot}} + V_{\text{ext}} \gamma_N^+ p_{\text{tot}} = \gamma_D^+ p_{\text{inc}}. \quad (41)$$

Defining the trace variable $\vartheta = \gamma_N^+ p_{\text{tot}}$ and using the transmission conditions (1), the continuous formulations read

$$\begin{bmatrix} \mathcal{F}_{\text{int}} & -\frac{\rho_{\text{int}}}{\rho_{\text{ext}}} I_{\text{int}} \\ \frac{1}{2}I_{\text{ext}} - K_{\text{ext}} & V_{\text{ext}} \end{bmatrix} \begin{bmatrix} p_{\text{int}} \\ \vartheta \end{bmatrix} = \begin{bmatrix} 0 \\ \gamma_D^+ p_{\text{inc}} \end{bmatrix} \quad (42)$$

where \mathcal{F}_{int} denotes the volumetric part of the the weak formulation (40) of the Helmholtz equation inside the heterogeneous subdomain. This FEM-BEM coupling is known as the Johnson-Nédélec variant [77, 78]. The discrete formulation on nonconforming meshes reads

$$\begin{bmatrix} \mathcal{F}_{\text{int}} & -\frac{\rho_{\text{int}}}{\rho_{\text{ext}}} F_e Z_{\text{int}}^{-1} Z_{\text{ext}} \\ \left(\frac{1}{2}I_{\text{ext}} - K_{\text{ext}}\right) Z_{\text{ext}}^{-1} Z_{\text{int}} F_r & V_{\text{ext}} \end{bmatrix} \begin{bmatrix} p_{\text{int}} \\ \vartheta \end{bmatrix} = \begin{bmatrix} 0 \\ \gamma_D^+ p_{\text{inc}} \end{bmatrix} \quad (43)$$

where the operators Z_{ext} and Z_{int} are the mortar operators (6) between the exterior mesh and the boundary of the volumetric mesh. Furthermore, the operators F_e and F_r denote the extension and restriction from the degrees of freedom in the interior to the degrees of freedom on the boundary of the volumetric mesh. The nonconforming technique can easily be extended to other formulations, including stabilised ones [79, 80].

4.2 Operator preconditioning

Operator preconditioning (cf. [81, 82]) effectively improves the convergence of linear solvers for the BEM [7, 83] and the boundary integral operators for the preconditioner are independently assembled from the model. For instance, Calderón and OSRC preconditioners for acoustic transmission [84] can be assembled on a coarser mesh than the boundary integral operators for the model itself. This idea is not restricted to acoustic transmission and is also valid for impenetrable objects discretised with strategies such as the OSRC-preconditioned Burton-Miller formulation [85] and opposite-order preconditioning of single-layer and hypersingular operators [86].

As an example, let us consider a Neumann screen problem

$$\begin{cases} \Delta p_{\text{sca}} + k_{\text{ext}}^2 p_{\text{sca}} = 0, & \text{in } \Omega; \\ \gamma_N p_{\text{sca}} = -\gamma_N p_{\text{inc}}, & \text{on } \Gamma; \\ \lim_{\mathbf{r} \rightarrow \infty} |\mathbf{r}|(\partial_{|\mathbf{r}|} p_{\text{sca}} - \imath k_{\text{ext}} p_{\text{sca}}) = 0; \end{cases} \quad (44)$$

where Γ is an open two-dimensional manifold in the three-dimensional domain Ω . The boundary integral formulation reads

$$\begin{cases} D_{\text{ext}} \phi = \gamma_N u_{\text{inc}}, & \text{on } \Gamma; \\ u_{\text{sca}} = \mathcal{K}_{\text{ext}} \phi, & \text{in } \Omega. \end{cases} \quad (45)$$

Opposite-order preconditioning suggests the use of the single-layer integral operator as preconditioner [86], even in the case of screen problems where boundary singularities occur [87]. The preconditioner does not need to have the same wavenumber or be assembled with the same numerical parameters as the original matrix [88, 89]. Hence,

$$Z_{\text{ext}}^{-1} Z_{\text{int}} V_{\text{int}} Z_{\text{int}}^{-1} Z_{\text{ext}} D_{\text{ext}} \phi = Z_{\text{ext}}^{-1} Z_{\text{int}} V_{\text{int}} Z_{\text{int}}^{-1} Z_{\text{ext}} \gamma_N u_{\text{inc}} \quad (46)$$

is a valid preconditioning strategy, where the model is assembled on an ‘exterior’ mesh and the preconditioner on a coarser ‘interior’ mesh.

5 Results

This section presents numerical benchmarks of the nonconforming BEM on canonical test cases and a large-scale model of an acoustic foam.

5.1 Computational framework

The weak formulation of the BEM uses local P1 elements on a triangular surface mesh. Even though accelerators can readily be applied to the proposed technology, dense matrix arithmetic is used to limit the parameter space of the benchmarks. The surface integrals are numerically evaluated with quadrature rules of order four, with semi-analytical transformations to handle singularities [6]. The GMRES algorithm [90] solves the linear system, without restart and a termination criterion of 10^{-5} . Table 1 summarises the boundary integral formulations for this study and mass matrix preconditioning is always applied since it improves the convergence of GMRES with little computational overhead.

The BEM was implemented with Bempp-cl (version 0.2.4) [91] and the FEM with Fenics (version 2019.1) [92]. The meshes were generated with Gmsh (version 4.9.5) [93]. The open-source Matlab code of the PANG algorithm [73] and the PANG2 patch [75] were rewritten into Python for compatibility with Bempp-cl and Fenics.

Shared-memory parallelisation was automatically performed through the Py-OpenCL (version 2022.1) [94] implementation of Bempp-cl for matrix assembly, Numpy (version 1.21.5) [95] for dense matrix algebra, Scipy (version 1.8) [96] for sparse matrix algebra, Numba (version 0.55.1) [94] for the PANG, and Joblib (version 1.1) [97] for independent mortar matrices. All simulations were performed on a computer with two Intel(R) Xeon(R) CPU E5-2640 v4 @ 2.40 GHz processors, 20 cores, 40 threads, and 512 GB shared memory.

5.2 Projection accuracy

The mortar matrices introduce a projection error when mapping between functions defined on P1 elements at nonconforming grids. On a continuous level,

Table 1: Overview of the boundary integral formulations for acoustic transmission problems. The version refers to the unknown surface potentials being exterior or interior traces. The number of operators refers to dense boundary integral operators only. The number of potentials refers to the unknown surface potentials.

formulation	version	equation	#operators	#potentials
PMCHWT	exterior	(18)	8	2
PMCHWT	interior	(21)	8	2
Müller	exterior	(19)	8	2
Müller	interior	(22)	8	2
multiple-traces	-	(13)	8	4
high-contrast	exterior Neumann	(25)	4	2
high-contrast	exterior Dirichlet	(27)	4	2
high-contrast	interior Neumann	(29)	4	2
high-contrast	interior Dirichlet	(31)	4	2

the projection operators (6) satisfy

$$\begin{aligned} Z_{\text{int}}^{-1} Z_{\text{ext}} Z_{\text{ext}}^{-1} Z_{\text{int}} &= I_{\text{int}}, \\ Z_{\text{ext}}^{-1} Z_{\text{int}} Z_{\text{int}}^{-1} Z_{\text{ext}} &= I_{\text{ext}}. \end{aligned}$$

Hence, let us define the projection error of the mortar algorithm as

$$E_{\text{int}} = \|\mathbf{I}_{\text{int}} - \mathbf{M}_{\text{int}}^{-1} \mathbf{P}_{\text{int,ext}} \mathbf{M}_{\text{ext}}^{-1} \mathbf{P}_{\text{ext,int}}\|, \quad (47a)$$

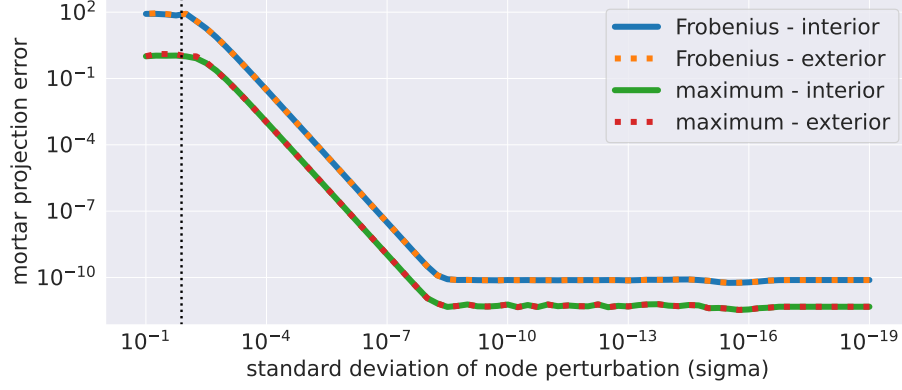
$$E_{\text{ext}} = \|\mathbf{I}_{\text{ext}} - \mathbf{M}_{\text{ext}}^{-1} \mathbf{P}_{\text{ext,int}} \mathbf{M}_{\text{int}}^{-1} \mathbf{P}_{\text{int,ext}}\|, \quad (47b)$$

corresponding to the interior and exterior mesh, respectively.

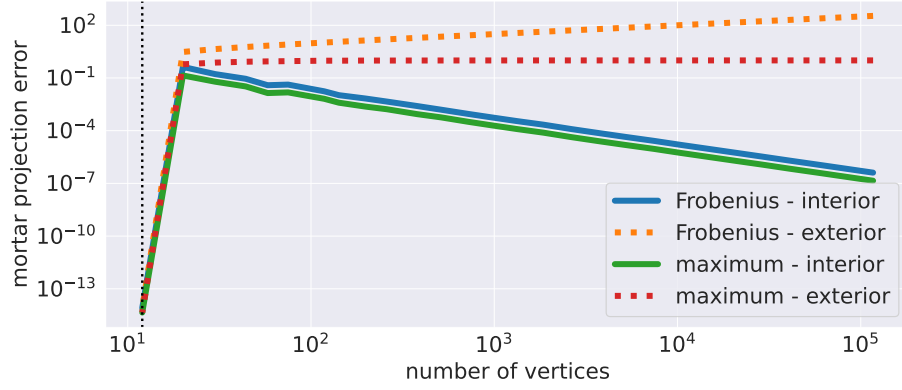
When both meshes are exactly the same, the projection error should be zero, except for rounding errors. Therefore, when a nonconforming mesh converges to the other mesh, the projection error is expected to converge to zero. Let us test this hypothesis on a triangular surface mesh for the unit square $[0, 1] \times [0, 1]$. The ‘interior’ grid is fixed and ‘exterior’ grids are generated from random perturbations of the nodes, drawn from a $\mathcal{N}(0, \sigma)$ distribution. To keep the same physical geometry, the inner nodes are perturbed in two dimensions, the boundary nodes only along the boundary, and the corner nodes not at all.

Figure 2a depicts the projection error, in the Frobenius and maximum norm. All four variants of the projection error decay quickly with smaller perturbations and flatten out when machine precision is reached. Hence, this experiment confirms the robustness of the PANG2 algorithm in finite precision arithmetic.

The two meshes in previous example have the same size but different configuration. Let us test the nonconforming projection with mesh refinement. Figure 2b shows the results when a fixed ‘interior’ mesh with $h = 0.5$ and 12 vertices is combined with an ‘exterior’ mesh that has an increasingly higher resolution. The finest mesh has $h = 0.0063$ and 116 746 nodes at the unit square



(a) The projection error (47) with respect to node perturbation with Gaussian noise having standard deviation σ in the ‘exterior’ mesh. The vertical line visualises the mesh width of $h = 0.013$ of the fixed ‘interior’ mesh, corresponding to 7044 nodes.



(b) The projection error (47) with respect to an increasingly fine ‘exterior’ mesh. The vertical line visualises the 12 vertices of the fixed ‘interior’ mesh.

Figure 2: The error of the mortar projection between nonconforming meshes.

$[0, 1] \times [0, 1]$. The leftmost data point in the line plot corresponds to equal mesh sizes and yields a projection error in the order of the machine precision. When refining the ‘exterior’ mesh, the interior projection error (47a) decreases while the exterior projection error (47b) increases. This deterioration in projection accuracy might be due to the passage from a high-dimensional space to a low-dimensional space and back to the high-dimensional space, thus losing precision in the dimension reduction.

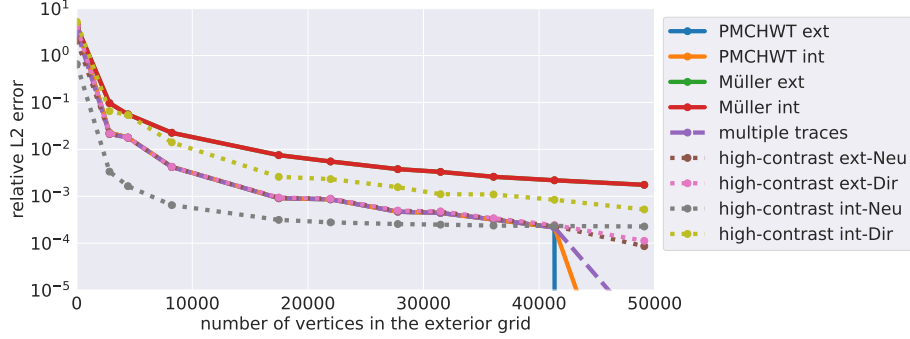
5.3 Accuracy of nonconforming BEM

It is common practice to generate meshes for the BEM based on a fixed number of elements per wavelength. While conforming BEM uses a mesh corresponding to the smallest wavelength across the interface, nonconforming BEM is applicable to meshes based on the wavenumber in each subdomain. This reduction in degrees of freedom at the same frequency is one of the key advantages of the nonconforming BEM. On the downside, nonconforming BEM introduces inaccuracies in the mortar projection. Hence, let us test the accuracy of the nonconforming BEM on a cube of size $[0, 1] \times [0, 1] \times [0, 1]$. The incident plane wave field travels in the positive x -direction, i.e.,

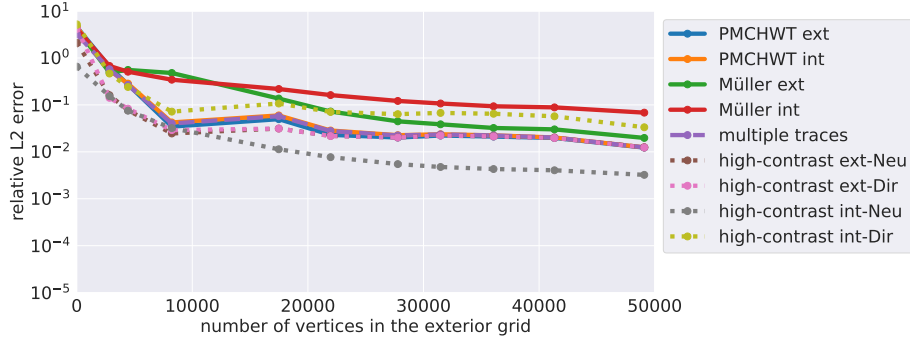
$$u_{\text{inc}}(\mathbf{x}) = e^{i \frac{2\pi f}{c_{\text{ext}}} \mathbf{x} \cdot \mathbf{d}} \quad \text{for } \mathbf{x} \in \mathbb{R}^3 \text{ and } \mathbf{d} = \begin{bmatrix} 1 \\ 0 \\ 0 \end{bmatrix}. \quad (48)$$

The physical parameters are chosen as $f = 1$, $c_{\text{ext}} = 0.3$, $c_{\text{int}} = 1.1$, $\rho_{\text{ext}} = 1$, and $\rho_{\text{int}} = 2$. In this case, the wavelengths are $\lambda_{\text{ext}} = 0.3$ and $\lambda_{\text{int}} = 1.1$ and the wavenumbers are $k_{\text{ext}} = 20.9$ and $k_{\text{int}} = 5.7$. These values compare to the unit cube with nondimensional edge lengths equal to one. The acoustic field is calculated on a grid of 100×100 points uniformly located in the square $[-0.5, 1.5] \times [-0.5, 1.5]$ on the plane $z = 0.5$. No analytical solution is available for a cube and the accuracy is defined as the relative ℓ_2 norm of the difference between the simulation and a reference solution. Specifically, the exterior PMCHWT formulation on a mesh with $h_{\text{ext}} = h_{\text{int}} = 0.012$ and 49,098 vertices, corresponding to at least 25 elements per wavelength, provides the reference solution. The benchmark uses $h_{\text{ext}} = h_{\text{int}}$ for conforming BEM and $\lambda_{\text{ext}}/h_{\text{ext}} = \lambda_{\text{int}}/h_{\text{int}}$ (a constant number of elements per wavelength) for nonconforming BEM. All meshes are independently created with different resolution.

Figure 3 confirms that the acoustic fields improve with mesh refinement. The nonconforming BEM is not as accurate as the conforming BEM due to the additional mortar projection errors. However, it requires considerably less degrees of freedom and is thus beneficial for fast simulations that do not require high accuracy. The differences between boundary integral formulations strongly depend on the benchmark considered (cf. [7]) and its comparison is outside the scope of this study.



(a) The accuracy of the BEM formulations for conforming meshes. The finest mesh in the convergence study corresponds to the reference simulation.



(b) The accuracy of the BEM formulations for nonconforming meshes. The pair of finest meshes has 49,098 and 3788 nodes for the exterior and interior grid, respectively.

Figure 3: The accuracy of the BEM with mesh refinement. The relative error is the difference with respect to the conforming exterior PMCHWT formulation with 49,098 vertices in the mesh.

5.4 Computational efficiency

The Bempp-cl library provides multithreaded calculations through a PyOpenCL implementation for the assembly of the discrete boundary integral operators. The PANG cannot be parallelised easily since it is an advancing front method that recursively calculates mortar contributions of neighbouring elements. However, the assembly of the mortar projection on each plane manifold of the polyhedral geometry (for example, the six faces of a cube) are independent and each task can be performed in parallel. The efficiency of the Python implementation of the mortar matrices was improved by the following approaches. Firstly, the mortar matrices satisfy $\mathbf{P}_{\text{ext,int}} = \mathbf{P}_{\text{int,ext}}^T$ so that only one of the two mortar matrices needs to be assembled. Secondly, the mortar matrix is assembled in the sparse coordinates (COO) format and then converted to a compressed-sparse-row (CSR) format for fast matrix-vector multiplications. Thirdly, the

assembly of the mortar matrices on each plane manifold is implemented with the Joblib package and task-based parallelism. Fourthly, the PANG algorithm was implemented with Numba acceleration.

Let us test the efficiency of the nonconforming BEM on three benchmarks. The first is the same as in Figure 3, the second has a three times higher frequency, and the third a three times higher material contrast, as summarised in Table 2. The third benchmark has a nine times lower exterior density so that the bulk modulus remains constant. While a change in density does not directly influence the mesh resolution, it does influence the conditioning of the linear system [72]. The grids consider six elements per wavelength and the mesh statistics are presented in Table 3.

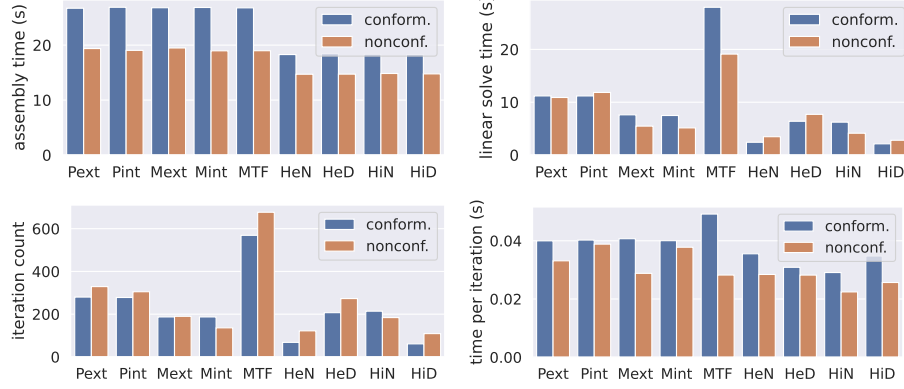
Table 2: Physical parameters for the efficiency benchmarks on the unit cube.

benchmark	f	c_{ext}	c_{int}	ρ_{ext}	ρ_{int}	k_{ext}	k_{int}
standard	1	0.3	1.1	1	2	20.9	5.7
high frequency	3	0.3	1.1	1	2	62.8	17.1
high contrast	1	0.1	1.1	0.11	2	62.8	5.7

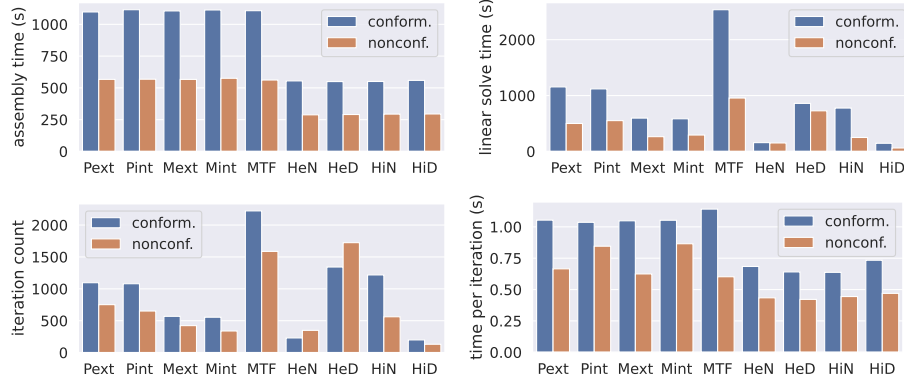
Table 3: Statistics of the meshes used in the efficiency benchmarks on the unit cube.

benchmark	both		conforming			nonconforming		
	h_{ext}	N_{ext}	h_{int}	N_{int}	N_{nodes}	h_{int}	N_{int}	N_{nodes}
standard	0.05	2836	0.05	2836	5672	0.183	272	3108
high frequency	0.017	25,302	0.017	25,302	50,604	0.061	2072	27,374
high contrast	0.017	25,302	0.017	25,302	50,604	0.183	272	25,574

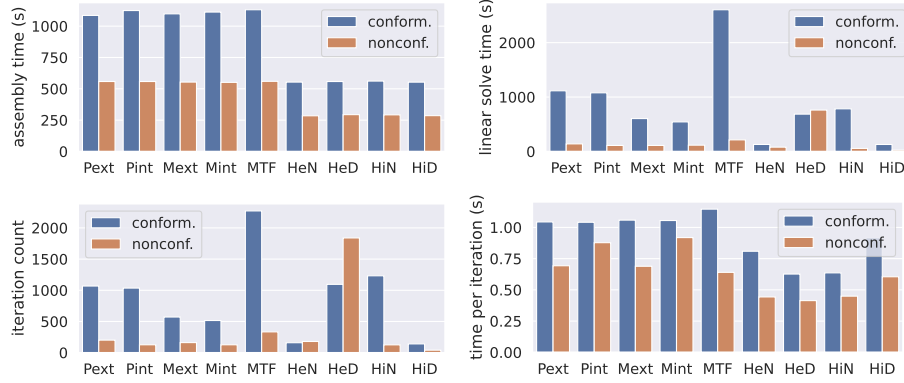
Figure 4 presents the wall-clock time of the different benchmarks and methodologies. The direct formulations involve a full set of eight boundary integral operators, while the high-contrast formulations require four dense operators only. This halves the assembly time. The assembly time for the nonconforming BEM is almost two times faster because the interior mesh has around ten times fewer nodes, and the matrices have around a hundred times fewer elements. Hence, the assembly time of the interior operators is not significant in the overall performance. This reduction in the number of degrees of freedom also explains the differences in the time per GMRES iteration: high-contrast is faster than direct formulations and nonconforming is faster than conforming BEM. However, the differences are diluted due to each iteration’s vector operations and preconditioning. The time to solve the system is dominated by the iteration count, and the differences between conforming and nonconforming BEM depend on the benchmark parameters and the boundary integral formulation. In many cases, nonconforming BEM improves the iteration count, on top of a reduction in time per iteration.



(a) The benchmark with standard physical parameters.



(b) The benchmark with high frequency.



(c) The benchmark with high material contrast.

Figure 4: The efficiency statistics of the nonconforming BEM, for all formulations in Table 1.

The timings include both the boundary integral operators and the mortar matrices. Looking into the breakdown, the BEM operators dominate the overall performance. The nonconforming routines never exceed 3% of the assembly time and 6% of the linear solve. These small contributions are because the mortar matrix is sparse, and the boundary integral operators are dense. Notice that acceleration with fast multipole methods or hierarchical matrix compression can speed up the dense arithmetic. However, their efficiency strongly depends on the specific implementation and parameter settings. While straightforward to apply accelerators to the nonconforming BEM, they are not considered in this study to limit the parameter space of the benchmarks.

Comparing the benchmark with standard physical parameters (Fig. 4a) to the more challenging high-frequency (Fig. 4b) and high-contrast (Fig. 4c) benchmarks, there is a significant gain in computation time for the nonconforming approach. At the challenging benchmarks, the nonconforming BEM relatively saves more nodes in the mesh, which has a quadratic influence on the size of the system matrix. Furthermore, nonconforming BEM reduces the iteration count considerably for the high-frequency and high-contrast benchmarks. Hence, the overall computation time of the nonconforming BEM is a fraction of the conforming BEM.

5.5 FEM-BEM coupling

Section 4.1 explained the nonconforming algorithm for FEM-BEM coupling. As in the case of pure BEM, advantages include independent mesh generation and reducing the degrees of freedom for high contrasts in speed of sound across the materials. In contrast to pure BEM, another benefit of nonconforming FEM-BEM coupling is the opportunity to use different grid resolutions proportional to the frequency for FEM and BEM. That is, while BEM only needs six elements per wavelength [98], the FEM needs a higher resolution [99] to achieve accurate results in practice [100]. Furthermore, the pollution effect in the FEM at high frequencies requires disproportionately more linear elements per wavelength [101], or adaptive high-order polynomial elements [102]. The pollution effect has not been observed to be as restrictive for the BEM as it is for the FEM, but its understanding and quantification remains an open discussion in literature [103, 104, 105]. In any case, the nonconforming algorithm allows for generating meshes with a different number of elements per wavelength for the BEM than for the FEM, allowing for more flexibility.

Let us test the nonconforming FEM-BEM coupling on a unit cube with a heterogeneous wavespeed. Specifically,

$$k_{\text{int}}(x, y, z) = k_{\text{ext}} (2 + \sin(2\pi x) \sin(2\pi y)), \quad (49)$$

$c_{\text{ext}} = 1$, $\rho_{\text{int}} = 1$, and $\rho_{\text{ext}} = 2$. Hence, the interior wavenumber is up to three times higher than in the exterior. Let us consider an incident plane wave (48) with $f = 2$, resulting in an exterior wavelength of $\lambda_{\text{ext}} = 0.5$ and $0.167 \leq \lambda_{\text{int}} \leq 0.5$ in the interior domain. These values are chosen proportional

to the nondimensional geometry, which is again a unit cube with edge lengths equal to one. The relatively high frequency and heterogeneous wavespeed necessitate a fine mesh for the FEM. The tetrahedral grid has 1,157,625 nodes with a maximum diameter of 0.01665 yielding at least ten elements per wavelength. The triangular surface mesh extracted from the volumetric mesh has 64,898 nodes and a maximum diameter of 0.01359, yielding at least 36 elements per exterior wavelength. The nonconforming FEM-BEM coupling uses the same FEM mesh but another BEM mesh with 5966 nodes and a maximum diameter of 0.04694, yielding at least 10 elements per exterior wavelength at the boundary.

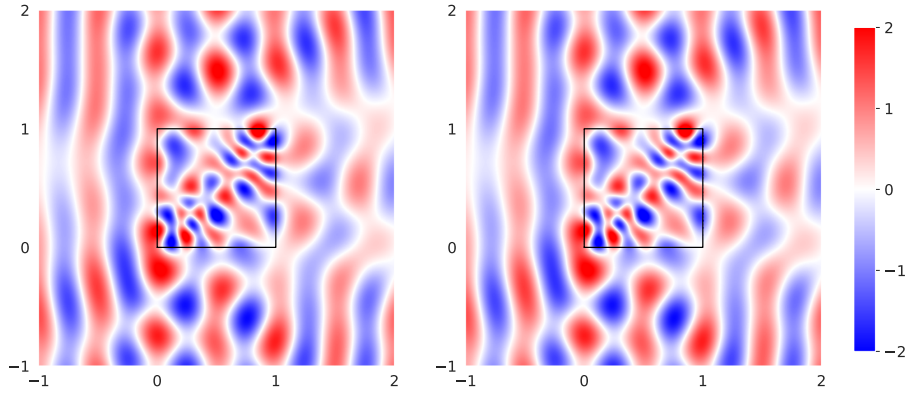


Figure 5: The real part of the acoustic field in the (x, y) -plane at $z = 0.5$ for an incident plane wave travelling in the positive x -direction. The black square depicts the boundary of the unit cube. The FEM-BEM coupled system uses conforming (left) or nonconforming (right) grids.

The standard FEM-BEM coupled formulation (43) is discretised with P1 elements for both the BEM and FEM. The BEM part is preconditioned with an inverse mass matrix and the FEM part with an incomplete LU factorisation, implemented with the SuperLU algorithm and default parameters [106]. The linear solver converged in 12,662 iterations for the nonconforming algorithm and in 13,961 iterations for the conforming FEM-BEM coupling. The GMRES solver was restarted every thousand iterations to reduce memory consumption. The entire simulation took five hours for the nonconforming and twelve hours for the conforming FEM-BEM algorithm. The acoustic field is depicted in Figure 5 and clearly shows the impact of a heterogeneous wavespeed in the interior. Also, the field from the conforming and nonconforming algorithm are almost identical, thus confirming the validity of the nonconforming FEM-BEM coupling.

5.6 Nonconforming operator preconditioning

The nonconforming algorithm is not limited to acoustic transmission and also applies to operator preconditioning at impenetrable domains, see Section 4.2.

Let us consider the Neumann problem (44) on a rectangular screen with corners at $(-0.25, -1, -1)$, $(0.25, 1, -1)$, $(0.25, 1, 1)$, and $(-0.25, -1, 1)$; having nondimensional edge lengths of 2 and 2.1. The propagating medium has $c_{\text{ext}} = 1$ and $\rho_{\text{ext}} = 1$, and the incident plane wave field propagates in the positive x -direction with frequency $f = 15$ yielding $k_{\text{ext}} = 94.2$. The surface mesh has 87,712 nodes and at least six elements per wavelength. The nonconforming operator preconditioner takes a coarse mesh with 9934 nodes and at least two elements per wavelength. Figure 6 shows the field and Table 4 the timing characteristics. The single-layer operator reduces the iteration count drastically and is thus an effective preconditioner for the hypersingular operator. However, the assembly time almost doubles due to the assembly of another dense matrix. The nonconforming approach alleviates this issue: the assembly on the coarse mesh and the mortar matrices are swift, the number of iterations remains low, and the linear system is solved quickly. Nevertheless, the assembly dominates the solve time, and the overall gain in simulation time is limited compared to mass-matrix preconditioning.

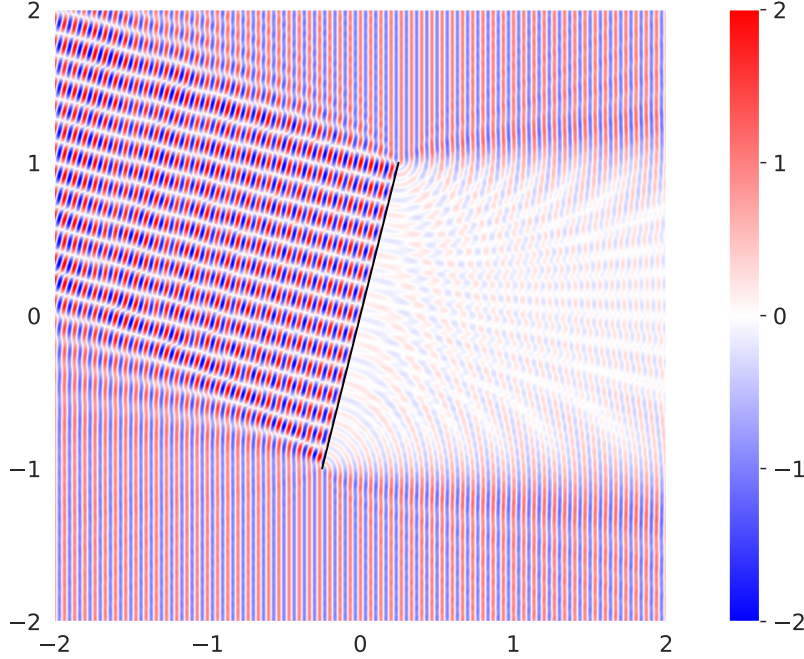


Figure 6: The real part of the acoustic field in the (x, y) -plane at $z = 0$, calculated with nonconforming operator-preconditioned BEM. The black line depicts the slice of the screen, which is perpendicular to the visualisation plane.

Table 4: The computational efficiency of the mass-preconditioned and opposite-order (OO) operator-preconditioned BEM on a screen: iteration count of GMRES (#iter), wall-clock time of the simulation (T_{bem}), matrix assembly (T_{matrix}), linear solver (T_{solve}), and each iteration (T_{iter}) in seconds.

formulation	#iter	T_{bem}	T_{matrix}	T_{solve}	T_{iter}
mass preconditioner	72	2136	1928	197	2.73
conforming OO prec.	7	3612	3534	67	9.63
nonconforming OO prec.	7	2064	2028	25	3.53

5.7 Acoustic foam model

As a final simulation to assess the nonconforming BEM, let us consider a large-scale benchmark on a geometry representing an acoustic foam. The object has a thickness of 2 cm for the base layer, and each pyramid has a rectangular base of size 10×10 cm and a height of 7 cm. The pyramids are replicated 16×16 times in a regular grid in the horizontal direction. The incident field

$$u_{\text{inc}}(\mathbf{x}) = \frac{e^{i \frac{2\pi f}{c_{\text{ext}}} |\mathbf{x} - \mathbf{x}_{\text{source}}|}}{4\pi |\mathbf{x} - \mathbf{x}_{\text{source}}|} \quad \text{for } \mathbf{x} \neq \mathbf{x}_{\text{source}} \text{ and } \mathbf{x}_{\text{source}} = \begin{bmatrix} 0 \\ 0 \\ 0.15 \end{bmatrix} \quad (50)$$

is a point source located at 15 cm altitude in the middle of the foam, with frequency of $f = 3$ kHz, which is at the higher end of the audible range. The exterior medium has material parameters $c_{\text{ext}} = 340$ m/s and $\rho_{\text{ext}} = 1.225$ kg/m³ that represent air. The interior medium represents a plastic foam, where attenuation was included as a power law for the complex wavenumber $k_{\text{int}} = 2\pi f/c_{\text{int}} + i\alpha_{\text{int}}f/f_{\alpha}$ with α the absorption coefficient [107]. The material parameters represent polyurethane [108]: $c_{\text{int}} = 1104$ m/s, $\rho_{\text{int}} = 1750$ kg/m³, and $\alpha_{\text{int}} = 7.5$ dB/cm = 86.3 Neper/m at $f_{\alpha} = 2$ MHz. The fine mesh has at least 5.7 elements per wavelength in the exterior and 18.5 in the interior. The coarse mesh has at least 7 elements per wavelength in the interior domain.

Figure 7 presents the acoustic field and Table 5 the efficiency characteristics of the different boundary integral formulations. Generally speaking, the nonconforming BEM improves the computational efficiency significantly. The assembly time almost halves, each iteration is quicker, and the iteration count is often lower than conforming BEM. The high-contrast interior Dirichlet formulation did not converge to the correct solution.

Overall, the results confirm the capacity of the nonconforming algorithm to improve the efficiency of the BEM for acoustic wave transmission. For example, the simulation time of the exterior PMCHWT reduces from 5:45 hours to 2:12 hours. Also, storing the dense matrices of all eight boundary integral operators in double precision takes at least 225 GByte for the conforming BEM and 115 GByte for the nonconforming BEM.

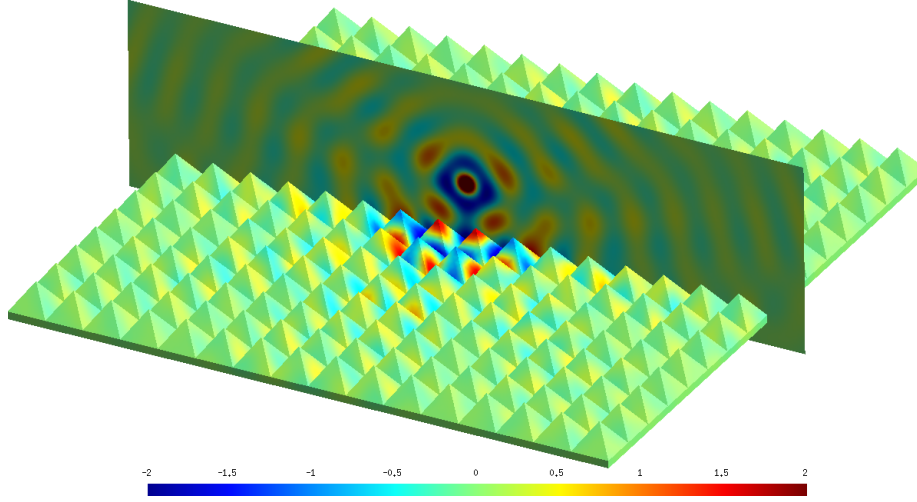


Figure 7: The real part of the acoustic field on the surface of the foam and on a slice through the point source, calculated with the nonconforming exterior PMCHWT formulation.

Table 5: The number of nodes in the meshes and the BEM's efficiency on the foam model: iteration count of GMRES ($\#iter$), wall-clock time of the assembly (T_{matrix}), linear solver (T_{solve}), and each iteration (T_{iter}) in seconds.

formulation	N_{ext}	N_{int}	$\#iter$	T_{matrix}	T_{solve}	T_{iter}
conforming BEM						
PMCHWT ext	43,469	43,469	4076	3478	17224	4.23
PMCHWT int	43,469	43,469	3838	3453	15296	3.99
Müller ext	43,469	43,469	4074	3616	19503	4.79
Müller int	43,469	43,469	3827	3403	13973	3.65
multiple-traces	43,469	43,469	8272	3378	34186	4.13
high-contrast ext Neu	43,469	43,469	175	1696	299	1.71
high-contrast ext Dir	43,469	43,469	2608	1690	4233	1.62
high-contrast int Neu	43,469	43,469	3268	1743	5363	1.64
nonconforming BEM						
PMCHWT ext	43,469	6707	3626	1745	6187	1.71
PMCHWT int	43,469	6707	1502	1747	3017	2.01
Müller ext	43,469	6707	3257	1783	5511	1.69
Müller int	43,469	6707	1356	1751	2740	2.02
multiple-traces	43,469	6707	6988	1767	12247	1.75
high-contrast ext Neu	43,469	6707	175	893	181	1.04
high-contrast ext Dir	43,469	6707	3927	933	4108	1.05
high-contrast int Neu	43,469	6707	1883	931	1933	1.03

6 Conclusions

The nonconforming BEM efficiently simulates acoustic transmission with independent surface meshes at the material interface. The mortar matrices that couple nonconforming surface meshes can be calculated quickly and robustly with an advancing front algorithm. Generating the grids is modular, with a fixed number of elements per wavelength in each domain, thus drastically reducing the number of degrees of freedom. The nonconforming algorithm works for any boundary integral equation, such as the single-trace, multiple-traces, and high-contrast formulations. Furthermore, the nonconforming algorithm improves FEM-BEM coupling and operator preconditioning for models involving heterogeneous or impenetrable structures.

The salient features of the nonconforming BEM include the flexibility in mesh generation and relaxed constraints on the mesh resolution. The computational benchmarks confirm a significant improvement in computational efficiency, reducing the calculation time of matrix assembly and matrix-vector products. On top of this, many benchmarks show faster convergence of the GMRES linear solver.

The downside of the nonconforming BEM is the introduction of projection errors between the meshes, which can be a limiting factor for high-accuracy simulations. Future research will consider the more advanced techniques proposed in the nonconforming FEM literature. Furthermore, the applicability of nonconforming BEM needs to be extended to geometries that have junctions with more than two subdomains, and curved surfaces where nonmatching grids are present.

Acknowledgements

This work was financially supported by the Agencia Nacional de Investigación y Desarrollo, Chile [FONDECYT 1230642].

References

- [1] D. Lahaye, J. Tang, and K. Vuik. *Modern Solvers for Helmholtz Problems*. Geosystems Mathematics. Birkhäuser, Cham, 2017.
- [2] Weng Cho Chew, Eric Michielssen, JM Song, and Jian-Ming Jin. *Fast and efficient algorithms in computational electromagnetics*. Artech House, Inc., Norwood, MA, 2001.
- [3] Jean-Claude Nédélec. *Acoustic and electromagnetic equations: integral representations for harmonic problems*, volume 144 of *Applied Mathematical Sciences*. Springer, New York, 2001.
- [4] Olaf Steinbach. *Numerical approximation methods for elliptic boundary value problems: finite and boundary elements*. Springer, New York, 2008.
- [5] George C Hsiao and Wolfgang L Wendland. *Boundary integral equations*, volume 164 of *Applied Mathematical Sciences*. Springer, Berlin, 2008.

- [6] Stefan A Sauter and Christoph Schwab. *Boundary Element Methods*, volume 39 of *Springer Series in Computational Mathematics*. Springer, Berlin, 2011.
- [7] Elwin van 't Wout, Seyyed R. Haqshenas, Pierre G  lat, Timo Betcke, and Nader Saffari. Benchmarking preconditioned boundary integral formulations for acoustics. *International Journal for Numerical Methods in Engineering*, 122(20):5873–5897, 2021.
- [8] Wojciech   migaj, Timo Betcke, Simon Arridge, Joel Phillips, and Martin Schweiger. Solving boundary integral problems with BEM++. *ACM Transactions on Mathematical Software (TOMS)*, 41(2):6, 2015.
- [9] Oscar P Bruno and Leonid A Kunyansky. A fast, high-order algorithm for the solution of surface scattering problems: basic implementation, tests, and applications. *Journal of Computational Physics*, 169(1):80–110, 2001.
- [10] Daipei Liu, Steffen Marburg, Christian Geweth, and Nicole Kessissoglou. Non-negative intensity for structures with inhomogeneous damping. *Journal of Theoretical and Computational Acoustics*, 27(01):1850050, 2019.
- [11] Leilei Chen, Ruhui Cheng, Shengze Li, Haojie Lian, Changjun Zheng, and St  phane PA Bordas. A sample-efficient deep learning method for multivariate uncertainty qualification of acoustic–vibration interaction problems. *Computer Methods in Applied Mechanics and Engineering*, 393:114784, 2022.
- [12] LL Chen, H Lian, Z Liu, Y Gong, CJ Zheng, and SPA Bordas. Bi-material topology optimization for fully coupled structural-acoustic systems with isogeometric FEM–BEM. *Engineering Analysis with Boundary Elements*, 135:182–195, 2022.
- [13] Cosmin Anitescu, Elena Atroshchenko, Naif Alajlan, and Timon Rabczuk. Artificial neural network methods for the solution of second order boundary value problems. *Computers, Materials and Continua*, 59(1):345–359, 2019.
- [14] Bernd Flemisch, Manfred Kaltenbacher, and Barbara I Wohlmuth. Elasto–acoustic and acoustic–acoustic coupling on non-matching grids. *International Journal for Numerical Methods in Engineering*, 67(13):1791–1810, 2006.
- [15] Charbel Farhat, Michael Lesoinne, and Patrick Le Tallec. Load and motion transfer algorithms for fluid/structure interaction problems with non-matching discrete interfaces: Momentum and energy conservation, optimal discretization and application to aeroelasticity. *Computer Methods in Applied Mechanics and Engineering*, 157(1-2):95–114, 1998.
- [16] Aukje de Boer, Alexander H van Zuijlen, and Hester Bijl. Review of coupling methods for non-matching meshes. *Computer Methods in Applied Mechanics and Engineering*, 196(8):1515–1525, 2007.
- [17] Armin Beckert and Holger Wendland. Multivariate interpolation for fluid-structure-interaction problems using radial basis functions. *Aerospace Science and Technology*, 5(2):125–134, 2001.
- [18] Peter Hansbo, Carlo Lovadina, Ilaria Perugia, and Giancarlo Sangalli. A Lagrange multiplier method for the finite element solution of elliptic interface problems using non-matching meshes. *Numerische Mathematik*, 100(1):91–115, 2005.
- [19] Thomas Kl  ppel, Alexander Popp, Ulrich K  ttler, and Wolfgang A Wall. Fluid–structure interaction for non-conforming interfaces based on a dual mortar formulation. *Computer Methods in Applied Mechanics and Engineering*, 200(45-46):3111–3126, 2011.

- [20] David E Keyes, Lois C McInnes, Carol Woodward, William Gropp, Eric Myra, Michael Pernice, John Bell, Jed Brown, Alain Clo, Jeffrey Connors, Emil Constantinescu, Don Estep, Kate Evans, Charbel Farhat, Ammar Hakim, Glenn Hammond, Glen Hansen, Judith Hill, Tobin Isaac, Xiangmin Jiao, Kirk Jordan, Dinesh Kaushik, Efthimios Kaxiras, Alice Koniges, Kihwan Lee, Aaron Lott, Qiming Lu, John Magerlein, Reed Maxwell, Michael McCourt, Miriam Mehl, Roger Pawlowski, Amanda P Randles, Daniel Reynolds, Beatrice Rivière, Ulrich Rüde, Tim Scheibe, John Shadid, Brendan Sheehan, Mark Shephard, Andrew Siegel, Barry Smith, Xianzhu Tang, Cian Wilson, and Barbara Wohlmuth. Multiphysics simulations: Challenges and opportunities. *The International Journal of High Performance Computing Applications*, 27(1):4–83, 2013.
- [21] Tayfun E Tezduyar. Finite element methods for flow problems with moving boundaries and interfaces. *Archives of Computational Methods in Engineering*, 8(2):83–130, 2001.
- [22] G Houzeaux, JC Cajas, Marco Discacciati, B Eguzkitza, A Gargallo-Peiró, M Rivero, and M Vázquez. Domain decomposition methods for domain composition purpose: Chimera, overset, gluing and sliding mesh methods. *Archives of Computational Methods in Engineering*, 24(4):1033–1070, 2017.
- [23] Joris Degroote. Partitioned simulation of fluid-structure interaction. *Archives of Computational Methods in Engineering*, 20(3):185–238, 2013.
- [24] Bernd Flemisch, Manfred Kaltenbacher, Simon Triebenbacher, and Barbara Wohlmuth. Non-matching grids for a flexible discretization in computational acoustics. *Communications in Computational Physics*, 11(2):472–488, 2012.
- [25] Martin Healey and Norbert Heuer. Mortar boundary elements. *SIAM Journal on Numerical Analysis*, 48(4):1395–1418, 2010.
- [26] Kristof Cools. Mortar boundary elements for the EFIE applied to the analysis of scattering by PEC junctions. In *2012 Asia-Pacific Symposium on Electromagnetic Compatibility*, pages 165–168, Singapore, 2012. IEEE.
- [27] K Cools. A mortar element method for the electric field integral equation on sheets and junctions. In *Computational Electromagnetics—Retrospective and Outlook*, pages 167–184. Springer, Singapore, 2015.
- [28] Zhen Peng, Ralf Hiptmair, Yang Shao, and Brian MacKie-Mason. Domain decomposition preconditioning for surface integral equations in solving challenging electromagnetic scattering problems. *IEEE Transactions on Antennas and Propagation*, 64(1):210–223, 2015.
- [29] Kui Han, Yongpin Chen, Xiaofeng Que, Ming Jiang, Jun Hu, and Zaiping Nie. A domain decomposition scheme with curvilinear discretizations for solving large and complex PEC scattering problems. *IEEE Antennas and Wireless Propagation Letters*, 17(2):242–246, 2017.
- [30] Yongpin Chen, Dongwei Li, Jun Hu, and Jin-Fa Lee. A nonconformal surface integral equation for electromagnetic scattering by multiscale conducting objects. *IEEE Journal on Multiscale and Multiphysics Computational Techniques*, 3:225–234, 2018.
- [31] Beibei Kong, Xiao-Wei Huang, and Xin-Qing Sheng. A discontinuous Galerkin surface integral solution for scattering from homogeneous objects with high dielectric constant. *IEEE Transactions on Antennas and Propagation*, 68(1):598–603, 2019.

- [32] Bo Mi, Yu Hu, Zhang Liu, and Ling Qin. Convergence of the interior penalty integral equation domain decomposition method. *Journal of Electronic Science and Technology*, 17(2):152–160, 2019.
- [33] Rui-Qing Liu, Xiao-Wei Huang, Yu-Lin Du, Ming-Lin Yang, and Xin-Qing Sheng. Massively parallel discontinuous Galerkin surface integral equation method for solving large-scale electromagnetic scattering problems. *IEEE Transactions on Antennas and Propagation*, 69(9):6122–6127, 2021.
- [34] Xiao-Wei Huang, Ming-Lin Yang, and Xin-Qing Sheng. A simplified discontinuous Galerkin self-dual integral equation formulation for electromagnetic scattering from extremely large IBC objects. *IEEE Transactions on Antennas and Propagation*, 70(5):3575–3586, 2022.
- [35] Franz Chouly and Norbert Heuer. A Nitsche-based domain decomposition method for hypersingular integral equations. *Numerische Mathematik*, 121(4):705–729, 2012.
- [36] Catalina Domínguez and Norbert Heuer. A posteriori error analysis for a boundary element method with nonconforming domain decomposition. *Numerical Methods for Partial Differential Equations*, 30(3):947–963, 2014.
- [37] Norbert Heuer and Gredy Salmerón. A nonconforming domain decomposition approximation for the Helmholtz screen problem with hypersingular operator. *Numerical Methods for Partial Differential Equations*, 33(1):125–141, 2017.
- [38] Catalina Domínguez, Ricardo Prato Torres, and Heidy González. An a posteriori error estimator for a non-conforming domain decomposition method for a harmonic elastodynamics equation. *East Asian Journal on Applied Mathematics*, 8(2):365–384, 2018.
- [39] Daniel L Dault, Naveen V Nair, Jie Li, and Balasubramaniam Shanker. The generalized method of moments for electromagnetic boundary integral equations. *IEEE Transactions on Antennas and Propagation*, 62(6):3174–3188, 2014.
- [40] Shifeng Huang, Gaobiao Xiao, Yuyang Hu, Rui Liu, and Junfa Mao. Multi-branch Rao-Wilton-Glisson basis functions for electromagnetic scattering problems. *IEEE Transactions on Antennas and Propagation*, 69(10):6624–6634, 2021.
- [41] Ting-Wen Wu. Multi-domain boundary element method in acoustics. In *Computational Acoustics of Noise Propagation in Fluids-Finite and Boundary Element Methods*, pages 367–386. Springer, 2008.
- [42] Zhen Peng, Kheng-Hwee Lim, and Jin-Fa Lee. Nonconformal domain decomposition methods for solving large multiscale electromagnetic scattering problems. *Proceedings of the IEEE*, 101(2):298–319, 2012.
- [43] Ran Zhao, Jun Hu, Huapeng Zhao, Ming Jiang, and Zai-ping Nie. Solving EM scattering from multiscale coated objects with integral equation domain decomposition method. *IEEE Antennas and Wireless Propagation Letters*, 15:742–745, 2016.
- [44] Ming Jiang, Jun Hu, Mi Tian, Ran Zhao, Xiang Wei, and Zaiping Nie. Solving scattering by multilayer dielectric objects using JMCIE-DDM-MLFMA. *IEEE Antennas and Wireless Propagation Letters*, 13:1132–1135, 2014.
- [45] Ran Zhao, Jun Hu, Huapeng Zhao, Ming Jiang, and Zaiping Nie. EFIE-PMCHWT-based domain decomposition method for solving electromagnetic scattering from complex dielectric/metallic composite objects. *IEEE Antennas and Wireless Propagation Letters*, 16:1293–1296, 2017.

- [46] Ran Zhao, Zhi Xiang Huang, Yongpin P Chen, and Jun Hu. Solving electromagnetic scattering from complex composite objects with domain decomposition method based on hybrid surface integral equations. *Engineering Analysis with Boundary Elements*, 85:99–104, 2017.
- [47] Ran Zhao, Hua Peng Zhao, Zai-ping Nie, and Jun Hu. Fast integral equation solution of scattering of multiscale objects by domain decomposition method with mixed basis functions. *International Journal of Antennas and Propagation*, 2015:563436, 2015.
- [48] Ran Zhao, Jun Hu, Huapeng Zhao, Ming Jiang, and Zaiping Nie. Fast solution of electromagnetic scattering from homogeneous dielectric objects with multiple-traces EF/MFIE method. *IEEE Antennas and Wireless Propagation Letters*, 16:2211–2215, 2017.
- [49] Ran Zhao, Zhixiang Huang, Wei-Feng Huang, Jun Hu, and Xianliang Wu. Multiple-traces surface integral equations for electromagnetic scattering from complex microstrip structures. *IEEE Transactions on Antennas and Propagation*, 66(7):3804–3809, 2018.
- [50] Ran Zhao, Jun Hu, Han Guo, Ming Jiang, and Zai-ping Nie. A hybrid solvers enhanced integral equation domain decomposition method for modeling of electromagnetic radiation. *International Journal of Antennas and Propagation*, 2015:467680, 2015.
- [51] Lan-Wei Guo, Yongpin Chen, Jun Hu, Joshua Le-Wei Li, and ZaiPing Nie. IE-DDM with a novel multiple-grid p-FFT for analyzing multiscale structures in half space. *Journal of Electromagnetic Waves and Applications*, 30(16):2138–2152, 2016.
- [52] Ming Jiang, Yongpin Chen, Dongwei Li, Huapeng Zhao, Sheng Sun, Zaiping Nie, and Jun Hu. A flexible SIE-DDM for EM scattering by large and multiscale problems. *IEEE Transactions on Antennas and Propagation*, 66(12):7466–7471, 2018.
- [53] Ulrich Langer and Olaf Steinbach. Boundary element tearing and interconnecting methods. *Computing*, 71(3):205–228, 2003.
- [54] Ulrich Langer and Olaf Steinbach. Coupled boundary and finite element tearing and interconnecting methods. In *Domain Decomposition Methods in Science and Engineering*, pages 83–97. Springer, Berlin, 2005.
- [55] Denny Fritze, Steffen Marburg, and Hans-Jürgen Hardtke. FEM–BEM-coupling and structural–acoustic sensitivity analysis for shell geometries. *Computers & structures*, 83(2-3):143–154, 2005.
- [56] Marinos Vouvakis, Kezhong Zhao, Seung-Mo Seo, and Jin-Fa Lee. A domain decomposition approach for non-conformal couplings between finite and boundary elements for unbounded electromagnetic problems in R3. *Journal of Computational Physics*, 225(1):975–994, 2007.
- [57] Thomas Rüberg and Martin Schanz. Coupling finite and boundary element methods for static and dynamic elastic problems with non-conforming interfaces. *Computer Methods in Applied Mechanics and Engineering*, 198(3-4):449–458, 2008.
- [58] Sascha Merz, Roger Kinns, and Nicole Kessissoglou. Structural and acoustic responses of a submarine hull due to propeller forces. *Journal of sound and vibration*, 325(1-2):266–286, 2009.

- [59] Herwig Peters, Steffen Marburg, and Nicole Kessissoglou. Structural-acoustic coupling on non-conforming meshes with quadratic shape functions. *International Journal for Numerical Methods in Engineering*, 91(1):27–38, 2012.
- [60] Tengfei Liang, Junpeng Wang, Jinyou Xiao, and Lihua Wen. Coupled BE–FE based vibroacoustic modal analysis and frequency sweep using a generalized resolvent sampling method. *Computer Methods in Applied Mechanics and Engineering*, 345:518–538, 2019.
- [61] Ping-Hao Jia, Lin Lei, Jun Hu, Yongpin Chen, Kui Han, Wei-Feng Huang, Zaiping Nie, and Qing Huo Liu. Twofold domain decomposition method for the analysis of multiscale composite structures. *IEEE Transactions on Antennas and Propagation*, 67(9):6090–6103, 2019.
- [62] Xianjin Li, Lin Lei, Yongpin Chen, Ming Jiang, Zaiping Nie, and Jun Hu. VSIE-based domain decomposition method with simplified prism vector basis functions for planar thin dielectric-conductor composite objects. *IEEE Antennas and Wireless Propagation Letters*, 17(9):1608–1612, 2018.
- [63] Y-Y Zhu, Q-M Cai, Runren Zhang, Xin Cao, Y-W Zhao, Bin Gao, and Jun Fan. Discontinuous Galerkin VSIE method for electromagnetic scattering from composite metallic and dielectric structures. *Progress In Electromagnetics Research M*, 84:197–209, 2019.
- [64] Xianjin Li, Lin Lei, Yongpin Chen, Ming Jiang, Ping-Hao Jia, Zhi Rong, Zaiping Nie, and Jun Hu. Solving EM scattering from complex thin dielectric/PEC composite targets by a VSIE-based method. *IEEE Transactions on Antennas and Propagation*, 68(5):3900–3910, 2020.
- [65] Xavier Claeys and Ralf Hiptmair. Multi-trace boundary integral formulation for acoustic scattering by composite structures. *Communications on Pure and Applied Mathematics*, 66(8):1163–1201, 2013.
- [66] A. J. Poggio and E. K. Miller. Integral equation solutions of three-dimensional scattering problems. In R. Mittra, editor, *Computer Techniques for Electromagnetics*, International Series of Monographs in Electrical Engineering, chapter 4, pages 159–264. Pergamon, Oxford, UK, 1973.
- [67] Yu Chang and Roger F Harrington. A surface formulation for characteristic modes of material bodies. Technical report, Syracuse University, Syracuse, NY, 10 1974. Technical Report TR-74-7.
- [68] Te-Kao Wu and Leonard L Tsai. Scattering from arbitrarily-shaped lossy dielectric bodies of revolution. *Radio Science*, 12(5):709–718, 1977.
- [69] Martin Costabel and Ernst Stephan. A direct boundary integral equation method for transmission problems. *Journal of Mathematical Analysis and Applications*, 106(2):367–413, 1985.
- [70] Claus Müller. *Grundprobleme der mathematischen Theorie elektromagnetischer Schwingungen*. Springer, Berlin, 1957.
- [71] R Kress and GF Roach. Transmission problems for the Helmholtz equation. *Journal of Mathematical Physics*, 19(6):1433–1437, 1978.
- [72] Elwin van ’t Wout, Seyyed R. Haqshenas, Pierre G  lat, Timo Betcke, and Nader Saffari. Boundary integral formulations for acoustic modelling of high-contrast media. *Computers & Mathematics with Applications*, 105:136–149, 2022.

- [73] Martin J Gander and Caroline Japhet. Algorithm 932: PANG: software for non-matching grid projections in 2D and 3D with linear complexity. *ACM Transactions on Mathematical Software (TOMS)*, 40(1):1–25, 2013.
- [74] Martin J Gander and Caroline Japhet. An algorithm for non-matching grid projections with linear complexity. In *Domain Decomposition Methods in Science and Engineering XVIII*, pages 185–192. Springer, 2009.
- [75] Conor McCoid and Martin J Gander. A provably robust algorithm for triangle-triangle intersections in floating-point arithmetic. *ACM Transactions on Mathematical Software (TOMS)*, 48(2):1–30, 2022.
- [76] Timo Betcke, Matthew W Scroggs, and Wojciech Śmigaj. Product algebras for Galerkin discretisations of boundary integral operators and their applications. *ACM Transactions on Mathematical Software (TOMS)*, 46(1):1–22, 2020.
- [77] Claes Johnson and J. Claude Nédélec. On the coupling of boundary integral and finite element methods. *Mathematics of Computation*, 35(152):1063–1079, 1980.
- [78] Francisco-Javier Sayas. The validity of Johnson–Nédélec’s BEM–FEM coupling on polygonal interfaces. *SIAM Journal on Numerical Analysis*, 47(5):3451–3463, 2009.
- [79] Elwin van ’t Wout. Stable and efficient FEM-BEM coupling with OSRC regularisation for acoustic wave transmission. *Journal of Computational Physics*, 450:110867, 2022.
- [80] Fabien Casenave, Alexandre Ern, and Guillaume Sylvand. Coupled BEM–FEM for the convected Helmholtz equation with non-uniform flow in a bounded domain. *Journal of Computational Physics*, 257:627–644, 2014.
- [81] Robert C Kirby. From functional analysis to iterative methods. *SIAM Review*, 52(2):269–293, 2010.
- [82] Ralf Hiptmair. Operator preconditioning. *Computers & Mathematics with Applications*, 52(5):699–706, 2006.
- [83] Stefan D Search, Christopher D Cooper, and Elwin van ’t Wout. Towards optimal boundary integral formulations of the Poisson-Boltzmann equation for molecular electrostatics. *Journal of Computational Chemistry*, 43(10):674–691, 2022.
- [84] Elwin van ’t Wout, Seyyed R. Haqshenas, Pierre Gélât, Timo Betcke, and Nader Saffari. Frequency-robust preconditioning of boundary integral equations for acoustic transmission. *Journal of Computational Physics*, 462:111229, 2022.
- [85] Elwin van ’t Wout, Pierre Gélât, Timo Betcke, and Simon Arridge. A fast boundary element method for the scattering analysis of high-intensity focused ultrasound. *The Journal of the Acoustical Society of America*, 138(5):2726–2737, 2015.
- [86] Olaf Steinbach and Wolfgang L Wendland. The construction of some efficient preconditioners in the boundary element method. *Advances in Computational Mathematics*, 9(1-2):191–216, 1998.
- [87] Oscar P Bruno and Stéphane K Lintner. A high-order integral solver for scalar problems of diffraction by screens and apertures in three-dimensional space. *Journal of Computational Physics*, 252:250–274, 2013.

- [88] Yassine Boubendir, Oscar Bruno, David Levadoux, and Catalin Turc. Integral equations requiring small numbers of Krylov-subspace iterations for two-dimensional smooth penetrable scattering problems. *Applied Numerical Mathematics*, 95:82–98, 2015.
- [89] Paul Escapil-Inchauspé and Carlos Jerez-Hanckes. Bi-parametric operator preconditioning. *Computers & Mathematics with Applications*, 102:220–232, 2021.
- [90] Youcef Saad and Martin H Schultz. GMRES: A generalized minimal residual algorithm for solving nonsymmetric linear systems. *SIAM Journal on Scientific and Statistical Computing*, 7(3):856–869, 1986.
- [91] Timo Betcke and Matthew W Scroggs. Bempp-cl: A fast Python based just-in-time compiling boundary element library. *Journal of Open Source Software*, 6(59):2879, 2021.
- [92] Anders Logg, Kent-Andre Mardal, and Garth Wells. *Automated solution of differential equations by the finite element method: The FEniCS book*, volume 84 of *Lecture Notes in Computational Science and Engineering*. Springer, Berlin, 2012.
- [93] Christophe Geuzaine and Jean-François Remacle. Gmsh: A 3-D finite element mesh generator with built-in pre- and post-processing facilities. *International Journal for Numerical Methods in Engineering*, 79(11):1309–1331, 2009.
- [94] Siu Kwan Lam, Antoine Pitrou, and Stanley Seibert. Numba: A LLVM-based Python JIT compiler. In *Proceedings of the Second Workshop on the LLVM Compiler Infrastructure in HPC*, pages 1–6, 2015.
- [95] Charles R Harris, K Jarrod Millman, Stéfan J Van Der Walt, Ralf Gommers, Pauli Virtanen, David Cournapeau, Eric Wieser, Julian Taylor, Sebastian Berg, Nathaniel J Smith, Robert Kern, Matti Picus, Stephan Hoyer, Marten H. van Kerkwijk, Matthew Brett, Allan Haldane, Jaime Fernández del Río, Mark Wiebe, Pearu Peterson, Pierre Gérard-Marchant, Kevin Sheppard, Tyler Reddy, Warren Weckesser, Hameer Abbasi, Christoph Gohlke, and Travis E. Oliphant. Array programming with NumPy. *Nature*, 585(7825):357–362, 2020.
- [96] Pauli Virtanen, Ralf Gommers, Travis E. Oliphant, Matt Haberland, Tyler Reddy, David Cournapeau, Evgeni Burovski, Pearu Peterson, Warren Weckesser, Jonathan Bright, Stéfan J. van der Walt, Matthew Brett, Joshua Wilson, K. Jarrod Millman, Nikolay Mayorov, Andrew R. J. Nelson, Eric Jones, Robert Kern, Eric Larson, C J Carey, İlhan Polat, Yu Feng, Eric W. Moore, Jake VanderPlas, Denis Laxalde, Josef Perktold, Robert Cimrman, Ian Henriksen, E. A. Quintero, Charles R. Harris, Anne M. Archibald, Antônio H. Ribeiro, Fabian Pedregosa, Paul van Mulbregt, and SciPy 1.0 Contributors. SciPy 1.0: Fundamental Algorithms for Scientific Computing in Python. *Nature Methods*, 17:261–272, 2020.
- [97] Joblib Development Team. Joblib: running Python functions as pipeline jobs, 2022. <https://joblib.readthedocs.io/>.
- [98] Steffen Marburg. Six boundary elements per wavelength: Is that enough? *Journal of Computational Acoustics*, 10(1):25–51, 2002.
- [99] P Langer, M Maeder, C Guist, M Krause, and S Marburg. More than six elements per wavelength: the practical use of structural finite element models and their accuracy in comparison with experimental results. *Journal of Computational Acoustics*, 25(04):1750025, 2017.

- [100] Jean-Francois Aubry, Oscar Bates, Christian Boehm, Kim Butts Pauly, Douglas Christensen, Carlos Cueto, Pierre G  lat, Llu  s Guasch, Jiri Jaros, Yun Jing, Rebecca Jones, Ningrui Li, Patrick Marty, Hazael Montanaro, Esra Neufeld, Samuel Pichardo, Gianmarco Pinton, Aki Pulkkinen, Antonio Stanziola, Axel Thielscher, Bradley Treeby, and Elwin van 't Wout. Benchmark problems for transcranial ultrasound simulation: Intercomparison of compressional wave models. *The Journal of the Acoustical Society of America*, 152(2):1003–1019, 2022.
- [101] Ivo M Babu  ka and Stefan A Sauter. Is the pollution effect of the FEM avoidable for the Helmholtz equation considering high wave numbers? *SIAM Journal on Numerical Analysis*, 34(6):2392–2423, 1997.
- [102] Th  ophile Chaumont-Frelet. On high order methods for the heterogeneous Helmholtz equation. *Computers & Mathematics with Applications*, 72(9):2203–2225, 2016.
- [103] Steffen Marburg. A pollution effect in the boundary element method for acoustic problems. *Journal of Theoretical and Computational Acoustics*, 26(02):1850018, 2018.
- [104] Wolfgang Kreuzer. Numerical simulation of sound propagation in and around ducts using thin boundary elements. *Journal of Sound and Vibration*, 534:117050, 2022.
- [105] Jeffrey Galkowski and Euan A Spence. Does the Helmholtz boundary element method suffer from the pollution effect? *SIAM Review*, 65(3):806–828, 2023.
- [106] Xiaoye S Li. An overview of SuperLU: Algorithms, implementation, and user interface. *ACM Transactions on Mathematical Software (TOMS)*, 31(3):302–325, 2005.
- [107] Steven L Garrett. *Understanding Acoustics: An Experimentalist’s View of Sound and Vibration*. Springer, Cham, 2020.
- [108] Moitreyee Sinha and Donald J Buckley. Acoustic properties of polymers. In James E. Mark, editor, *Physical Properties of Polymers Handbook*, chapter 60, pages 1021–1031. Springer, New York, 2007.